Solar Phys (2017) 292:56
DOI 10.1007/s11207-017-1074-7

VLA Measurements of Faraday Rotation through Coronal Mass Ejections

Jason E. Kooi[1,2] · **Patrick D. Fischer**[2] · **Jacob J. Buffo**[2] · **Steven R. Spangler**[2]

Received: 1 November 2016 / Accepted: 27 February 2017

Abstract Coronal mass ejections (CMEs) are large-scale eruptions of plasma from the Sun, which play an important role in space weather. Faraday rotation is the rotation of the plane of polarization that results when a linearly polarized signal passes through a magnetized plasma such as a CME. Faraday rotation is proportional to the path integral through the plasma of the electron density and the line-of-sight component of the magnetic field. Faraday-rotation observations of a source near the Sun can provide information on the plasma structure of a CME shortly after launch. We report on simultaneous white-light and radio observations made of three CMEs in August 2012. We made sensitive Very Large Array (VLA) full-polarization observations using 1 – 2 GHz frequencies of a constellation of radio sources through the solar corona at heliocentric distances that ranged from 6 – 15 $R_{\odot}$. Two sources (0842+1835 and 0900+1832) were occulted by a single CME, and one source (0843+1547) was occulted by two CMEs. In addition to our radioastronomical observations, which represent one of the first active hunts for CME Faraday rotation since Bird *et al.* (*Solar Phys.*, **98**, 341, 1985) and the first active hunt using the VLA, we obtained white-light coronagraph images from the *Large Angle and Spectrometric Coronagraph* (LASCO) C3 instrument to determine the Thomson-scattering brightness [B_T], providing a means to independently estimate the plasma density and determine its contribution to the observed Faraday rotation. A constant-density force-free flux rope embedded in the background corona was used to model the effects of the CMEs on B_T and Faraday rotation. The plasma densities ($6 – 22 \times 10^3$ cm^{-3}) and axial magnetic-field strengths (2 – 12 mG) inferred from our models are consistent with the modeling work of Liu *et al.* (*Astrophys. J.*, **665**, 1439, 2007) and Jensen and Russell (*Geophys. Res. Lett.*, **35**, L02103, 2008), as well as previous CME Faraday-rotation observations by Bird *et al.* (1985).

Keywords Corona · Coronal mass ejections · Magnetic fields, corona · Plasma physics · Polarization, radio · Others, Faraday rotation

✉ J.E. Kooi
jason.kooi@nrl.navy.mil

1 U.S. Naval Research Laboratory, Code 7213, 4555 Overlook Ave. SW, Washington, DC 20375, USA

2 Department of Physics and Astronomy, University of Iowa, Iowa City, IA, 52240, USA

Published online: 30 March 2017

1. Introduction

Coronal mass ejections (CMEs) are large-scale eruptions of plasma from the Sun, which play an important role in space weather. As technology continues to progress, the need for more reliable space-weather predictions has increased. The ejected material of a CME is associated with strong magnetic fields, which can cause substantial geomagnetic storms at Earth (Gosling *et al.*, 1991). The general picture of CME generation is as follows: magnetic-field lines emerge through the convection zone of the dense photosphere and into the more tenuous plasma of the corona, generating bipolar magnetic regions (Babcock, 1961). The complex motions of the photosphere adjust and twist these field lines, strengthening them until some non-equilibrium state is reached. After this, the magnetic energy is released and a CME erupts, carrying with it 10^{11} – 10^{13} kg of magnetized plasma at speeds from hundreds to over 1000 $\mathrm{km\,s^{-1}}$ (Chen, 2011).

While CMEs have many shapes and sizes, the standard CME is generally characterized by a closed outer loop and typically has a so-called three-part structure: a bright outer loop, followed by a dark cavity that contains a bright core (Illing and Hundhausen, 1985). The bright outer loop is usually identified with the expelled coronal mass, the cavity with a flux rope, and the bright core with the erupted prominence. Most other CME structures are believed to be a result of projection effects (Schwenn, 2006). When a normal CME is ejected near the center of the occulting disk of a coronagraph, it appears to surround the occulting disk, yielding what is known as a halo CME. When it is partially off-center, it will have an apparent angular width between 120° – 360°, earning the title partial halo CME. An exception to this is the narrow CME, which displays jet-like motions and is thought to be associated with open-field-line regions in the corona.

Although CMEs have been an active field of research since their discovery in the 1970s (*e.g.* MacQueen *et al.*, 1974; Gosling *et al.*, 1974; Brueckner, 1974), there is still much to understand. While the plasma structure of a CME is typically modeled as a magnetic-flux rope, there is no consensus on the effective trigger that initiates a CME. Other issues include identifying what causes the shift toward non-equilibrium and how CMEs are accelerated after initiation (see Chen, 2011, for more details).

Of particular importance for space-weather considerations is the orientation of the CME magnetic field with respect to the geomagnetic field of the Earth. Determining this orientation, however, is difficult. It is well known that the vector photospheric magnetic field can be determined by Zeeman splitting of spectral lines. Typical temperatures in CMEs range from 10^5 – 10^6 K; consequently, the plasma is highly ionized and tenuous, and therefore it is difficult to measure Zeeman splitting that is due to thermal and non-thermal broadening of the emission lines. Spacecraft near the first Lagrangian point (L_1) can measure local fields *in situ*, but these measurements would only allow a warning time of ≈ 30 minutes before arrival at Earth (Weimer *et al.*, 2002; Vogt *et al.*, 2006).

Observations of Faraday rotation, which is the rotation of the plane of polarization of linearly polarized radiation as it propagates through a magnetized plasma, have been used for decades to determine the strength and structure of the coronal magnetic field and plasma density. Beyond the quasi-static small-amplitude Faraday-rotation observations characteristic of the coronal plasma, large-amplitude transients associated with CMEs have also been detected and have the potential to improve our understanding of CMEs. Remote Faraday-rotation measurements can also be performed on Earth by tracking a CME from initiation to at least 15 $R_\odot$. Furthermore, Faraday rotation provides information on the orientation of the CME's magnetic field with respect to the observer's line of sight (LOS) and can potentially be used to determine this orientation well before the CME reaches Earth (Liu *et al.*, 2007).

Finally, Faraday-rotation observations of a source near the Sun could provide information on the plasma structure of a CME shortly after launch, potentially shedding light on the initiation process.

1.1. Faraday Rotation

This article deals with probing coronal mass ejections via Faraday rotation of radio waves from extragalactic radio sources. Faraday rotation is a change in the polarization position angle [χ] of polarized radiation as it propagates through a magnetized plasma; this rotation in position angle [$\Delta\chi$] is given by

$$\Delta\chi = \left[\left(\frac{e^3}{2\pi m_{\mathrm{e}}^2 c^4}\right)\int_{\mathrm{LOS}} n_{\mathrm{e}}\boldsymbol{B}\cdot \mathrm{d}\boldsymbol{s}\right]\lambda^2 = [\mathrm{RM}]\lambda^2 \tag{1}$$

in cgs units. In Equation (1), n_{e} and $\boldsymbol{B}$ are the plasma electron density and vector magnetic field, respectively. The fundamental physical constants in parentheses, e, m_e, and c are the fundamental charge, the mass of an electron, and the speed of light, respectively. The term in parentheses has the numerical value $C_{\mathrm{FR}} \equiv 2.631 \times 10^{-17}\ \mathrm{rad\,G^{-1}}$. $\mathrm{d}\boldsymbol{s}$ is an incremental vector representing the spatial increment along the LOS, which is the path on which the radio waves propagate with positive s is in the direction from the source to the observer. The subscript LOS on the integral indicates an integral along the LOS. Finally, λ indicates the wavelength of observation. The term in square brackets is called the rotation measure (hereafter denoted by the variable RM and reported in the SI units of $\mathrm{rad\,m^{-2}}$), and it is the physical quantity retrieved in Faraday-rotation measurements.

The geometry involved in a typical coronal Faraday-rotation measurement is illustrated in Figure 1. This figure illustrates two of the most important parameters for coronal Faraday rotation: the impact parameter [R_0], and the location of the magnetic neutral line along the LOS [β_{c}]. The impact parameter is the shortest heliocentric distance of any point along the LOS. The neutral line gives the location at which the polarity of the vector magnetic field reverses and is usually associated with the coronal current sheet. In Figure 1, the angle β is used as an equivalent variable to s for specifying the position along the LOS and is defined as positive toward the observer.

Faraday-rotation measurements of the coronal plasma can be made with either spacecraft transmitters or natural radio sources as the source of radio waves. Examples of results that have been obtained with spacecraft transmitters are given by Stelzried *et al.* (1970), Hollweg *et al.* (1982), Pätzold *et al.* (1987), Bird and Edenhofer (1990), Andreev *et al.* (1997), Jensen *et al.* (2013a, 2013b), and Efimov *et al.* (2015). Observations of natural radio sources typically use either pulsars or extragalactic sources. Observations using pulsars include Bird *et al.* (1980), Ord, Johnston, and Sarkissian (2007), and You *et al.* (2012), and observations using extragalactic radio sources include Sofue *et al.* (1972), Soboleva and Timofeeva (1983), Sakurai and Spangler (1994a, 1994b), Mancuso and Spangler (1999, 2000), Spangler (2005), Ingleby, Spangler, and Whiting (2007), Mancuso and Garzelli (2013), Le Chat *et al.* (2014), and Kooi *et al.* (2014). The advantage of using pulsars is that they can also be used to determine the dispersion delay through the corona simultaneously with Faraday rotation, thereby providing a means of independently estimating the plasma-density contribution to the rotation measure. The corresponding disadvantage is that the dispersion delay due to the corona and solar wind is small and cannot be measured with sufficient accuracy for most pulsars, with the exception of some millisecond pulsars (You *et al.*, 2012).

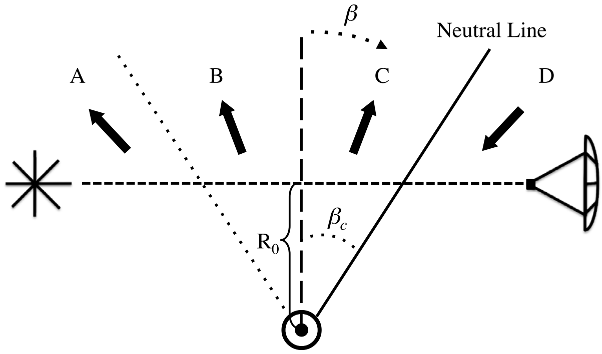

Figure 1 Illustration of the line of sight (LOS) from a radio source, through the corona, to a radio telescope on Earth. The LOS passes at a closest distance R_0 (impact parameter). The figure illustrates an idealization that is employed in this article: the background coronal magnetic field is radial (solid arrows). Faraday rotation depends sensitively on the location of the magnetic neutral line (solid line) along the LOS (given by the angle β_c). The dashed line divides the LOS into two halves of equal length, and the dotted line indicates a symmetry line. This symmetry is such that for the case of radial magnetic-field strength dependent only on heliocentric distance and spherically symmetric plasma density, the RM contributions from sectors B and C ($-\beta_c < \beta < \beta_c$) cancel each other out. This figure is a modified version of Figure 1 in Kooi *et al.* (2014) and has been adapted to coronal conditions in 2012 for 0846+1459 and 0843+1547.

1.2. White-Light Imaging of CMEs

In studying coronal Faraday rotation, it is important to remember that Faraday rotation yields a path-integrated measurement of the magnetic field and the plasma density. This presents two potential challenges. The first is that Faraday-rotation measurements depend on the components of the magnetic field parallel (or antiparallel) to the LOS; consequently, it is possible to measure zero Faraday rotation through the corona even when strong magnetic fields or dense plasmas are present. A simple example would be a purely unipolar radial magnetic field and $n_e = n_e(r)$ (*e.g.* see Kooi *et al.*, 2014). The second challenge is separating the contribution of the plasma density from the LOS magnetic field to the RM. The plasma density is typically determined independently from either models or observations.

In recent years, there have been considerable advances in space-based coronagraph technology, allowing for independent measurement of the coronal plasma density structure (*e.g.* see Jensen *et al.*, 2016). Modern observations of the corona are primarily obtained using white-light coronagraphs, which observe radiation from the photosphere that has been Thomson-scattered by electrons in the coronal plasma. The Thomson-scattering brightness [B_T] is directly related to the coronal electron density [n_e] by the LOS integral

$$B_T = \int_{LOS} n_e(\boldsymbol{r}) \mathcal{G}(\boldsymbol{r}) dr \tag{2}$$

where $\boldsymbol{r}$ is vector heliocentric distance and $\mathcal{G}(\boldsymbol{r})$ is a geometric function determined by assumptions about solar limb darkening and heliocentric distance. Provided that the geometric function $\mathcal{G}(\boldsymbol{r})$ is known, the plasma density can be calculated by inverting Equation (2). A more detailed discussion of $\mathcal{G}(\boldsymbol{r})$ appears in Section 3.1.1.

Over half a century ago, van de Hulst (1950) developed a method of deriving the coronal electron plasma density by inverting polarized-brightness measurements. Fifty years later, Hayes, Vourlidas, and Howard (2001) extended this technique to total-brightness observations, allowing them to take full advantage of the extensive *Large Angle and Spectrometric Coronagraph* (LASCO: Brueckner *et al.*, 1995) archive. Hayes, Vourlidas, and Howard

(2001) demonstrated that this total-brightness technique yielded results as robust as the traditional methods of deriving coronal electron densities; furthermore, total-brightness measurements allow electron densities to be calculated at heights and in conditions inaccessible to polarized-brightness observations. However, because the electron corona (K-corona) and scattering off interplanetary dust (F-corona) both contribute to the total brightness, the accuracy of deriving n_e from total-brightness observations depends strongly on the accuracy of the removal of the brightness contributions from the F-corona.

Total-brightness imaging of the corona has also been applied to studying coronal mass ejections (Vourlidas and Howard, 2006), providing information on many fundamental properties of CMEs, including mass (*e.g.* Colaninno and Vourlidas, 2009), speed and trajectory (*e.g.* Morrill *et al.*, 2009), and kinetic energy (*e.g.* Vourlidas *et al.*, 2010). These total-brightness techniques, originally developed for LASCO instruments onboard the *Solar and Heliospheric Observatory* (SOHO: Domingo, Fleck, and Poland, 1995), have also been extended to the *Sun-Earth Connection Coronal and Heliospheric Investigation* (SECCHI: Howard *et al.*, 2008) instrument suites onboard the twin *Solar TErrestrial RElations Observatory* (STEREO: Kaiser *et al.*, 2008) spacecraft. Individually, the white-light imagers on SOHO, STEREO-A, and STEREO-B have been used to develop large online CME catalogs that employ both manual detection methods, such as those used in the SOHO LASCO CME Catalog (Gopalswamy *et al.*, 2009), and automated-detection methods, as used in the Computer Aided CME Tracking software catalog (CACTus: Robbrecht, Berghmans, and Van der Linden, 2009) or the Solar Eruptive Event Detection System (SEEDS: Olmedo *et al.*, 2008).

However, the true power of these multiple white-light imaging instruments lies in combining measurements from SOHO, STEREO-A, and STEREO-B. Using white-light measurement of CMEs from these multiple vantage points, Mierla *et al.* (2010) reconstructed the three-dimensional structure of numerous single CME events from 2007 and 2008. Colaninno and Vourlidas (2015) similarly demonstrated the power of multiple-viewpoint observations by using SOHO, STEREO-A, and STEREO-B to reconstruct the three-dimensional structures of three overlapping and interacting CMEs to obtain insight into CME–CME interactions. However, these observational advances still rely on models for the CME plasma structure to determine the electron plasma density; furthermore, these white-light observations cannot provide direct measurements of the CME magnetic-field structure.

1.3. Previous Observations of CME Faraday Rotation

Most measurements of Faraday-rotation transients caused by CMEs have been made by observing spacecraft transmitters. Using *Pioneer* 6, Levy *et al.* (1969) made the first measurements of Faraday-rotation transients believed to be caused by CMEs in 1968 using an observational frequency of 2.292 GHz. During these observations, the authors measured three large W-shaped transients at different heliocentric distances (10.9 $R_\odot$, 8.6 $R_\odot$, and 6.2 $R_\odot$). The transients were $\approx 40^\circ$ (RM $\approx 41\ \mathrm{rad\,m^{-2}}$) in amplitude and lasted for two to three hours, and they were each preceded by radio (decametric) noise-burst events. Levy *et al.* (1969) did not determine a definitive source for these transients, but concluded that the events originated from a structure of significantly enhanced plasma density in the corona (*i.e.* they were not caused by ionospheric interference).

Cannon, Stelzried, and Ohlson (1973) made similar measurements of Faraday rotation in the corona using *Pioneer* 9, again at a frequency of 2.292 GHz. The authors observed two large transients. The first (located 5.9 $R_\odot$ West of the Sun) had essentially the same $\approx 40^\circ$ change in magnitude and the same negative rotation direction as the *Pioneer* 6 observations The second transient (located 6.2 $R_\odot$ East of the Sun) had a sigmoidal or inverse-N shape, decreasing by $\approx 7^\circ$, then increasing $\approx 7^\circ$ above the steady-state rotation angle ($|\mathrm{RM}| \approx 7.1\ \mathrm{rad\,m^{-2}}$) before leveling off over the course of five hours. The authors found flares or subflares that coincided with these two events and concluded that at least the first event probably resulted from the same type of phenomenon that caused the *Pioneer* 6 transients.

Whereas the previous measurements of coronal transients were fortuitous, Bird *et al.* (1985) made a concerted effort to detect this phenomenon. They used the *Solwind* coronagraph data to select intervals of Faraday-rotation and spectral-broadening measurements during solar occultations of *Helios* 1 and *Helios* 2 during October and November of 1979. They established a one-to-one correspondence between the five coronal transients observed in these two measurements and the passage of CMEs across the LOS. To date, these observations are the highest quality observations of Faraday-rotation anomalies due to CMEs. Because these transients were very similar to those observed by Levy *et al.* (1969), Pätzold and Bird (1998) concluded that CMEs were most likely responsible for the transients observed by Levy *et al.* (1969) as well.

Howard *et al.* (2016) detected CME Faraday rotation using a pulsar (PSR B0950+08) and were able to simultaneously derive dispersion measures for this source. While the heliocentric distances were comparable to previous measurements ($> 8.7\ \mathrm{R_\odot}$), Howard *et al.* (2016) measured a relatively weak Faraday-rotation signal, $3.6 - 4.3\ \mathrm{rad\,m^{-2}}$, that was comparable to their estimate for the ionospheric Faraday rotation, $1.5 - 2.5\ \mathrm{rad\,m^{-2}}$. Consequently, they provided upper limits on the density and LOS magnetic-field strength and did not attempt to model the CME plasma structure.

There is only one known measurement of a CME Faraday-rotation anomaly during observations of an extragalactic radio source. Spangler and Whiting (2009) indicated that the outer loop of a CME approached two sources (J2335-015 and J2337-025) during Faraday-rotation observations at 1.465 GHz performed by Ingleby, Spangler, and Whiting (2007). Although the LASCO-C2 coronagraph images suggested that the outer loop did not quite cross these LOS, the Faraday rotation of J2337-025 monotonically increased in time, increasing by $\approx 26^\circ$ ($\mathrm{RM} \approx 10.9\ \mathrm{rad\,m^{-2}}$) by the end of the observing session.

1.4. Flux-Rope Modeling of CMEs

One of the models that has become standard in describing CME morphologies is the flux rope. *In-situ* measurements of CMEs using several spacecraft (*e.g. Voyager* 1, *Voyager* 2, *Helios* 1, *Helios* 2, and IMP 8) indicate that magnetic fields threading CMEs take the form of a helical flux-rope (Burlaga *et al.*, 1981; Burlaga, 1988; Lepping, Burlaga, and Jones, 1990). This flux rope is either developed as part of the supporting structure necessary for the initial development of the solar prominence, or it is developed as a result of field lines reconnecting during the eruption. In addition to the spacecraft observations, the flux rope configuration also explains the white-light structure of CMEs (Chen, 1996; Gibson and Low, 1998; Gibson and Low, 2000). Gibson *et al.* (2006) reported a more recent comprehensive survey of white-light quiescent cavities (associated with a range of coronal-loop morphologies) that suggested that the flux-rope structure is formed prior to initiation of the CME.

Most models of CMEs describe the inner cavity as a flux rope (Low, 2001); however, in forward modeling of CMEs captured by white-light imaging, the flux-rope structure has also been used to describe the enhanced density structure of the bright outer loop preceding the inner cavity. Thernisien, Howard, and Vourlidas (2006) modeled CMEs observed by the SECCHI-COR2 instruments on STEREO-A and STEREO-B using a graduated cylindrical shell (GCS) flux-rope structure in which the electrons are placed near the surface. Wood *et al.* (2009) similarly used a flux-rope-like structure in modeling two distinct fronts of a

CME on 17 May 2008. Both Thernisien, Howard, and Vourlidas (2006) and Wood *et al.* (2009) successfully reproduced the observed CME morphologies and determined electron densities (at the CME front) for these events. More recently, Colaninno and Vourlidas (2015) used the GCS model to fit observations of three interacting CMEs and inferred the trajectories, orientations, velocities, and source regions of these CMEs.

As mentioned previously, the orientation of the magnetic field is important in understanding the potential effects of a CME impacting the Earth's magnetosphere. Liu *et al.* (2007) have demonstrated that Faraday-rotation measurements provide a remote-sensing method for determining this orientation well in advance of a CME's arrival at Earth. They simulated Faraday-rotation measurements using force-free ($\nabla \times \boldsymbol{B} = \alpha \boldsymbol{B}$) and non-force-free magnetic-flux ropes and found that both types can i) reproduce the signs and magnitudes of Faraday-rotation transients previously associated with CMEs and ii) produce the same range in Faraday-rotation profiles, from pseudo-Gaussian to N-shaped profiles. More importantly, the authors simulated a two-dimensional Faraday sky map of a flux-rope CME approaching Earth and argued that the full orientation and helicity of the CME could be remotely determined by Faraday-rotation measurements using multiple LOS.

Building on this approach, Jensen and Russell (2008) attempted to reproduce the observational results of Levy *et al.* (1969), Cannon, Stelzried, and Ohlson (1973), and Bird *et al.* (1985) using force-free flux ropes. Jensen and Russell (2008) were able to reproduce the general V-shape of the Faraday-rotation profiles, but they could not reproduce the middle hump of the W shape of the *Pioneer* 6 and *Helios* observations. While they did not explore this discrepancy, Liu *et al.* (2007) did note that two adjacent flux ropes with evolving fields could yield a W-shaped profile. Both Liu *et al.* (2007) and Jensen and Russell (2008) found that multiple LOS are necessary for resolving any ambiguities in the magnetic-field orientation or helicity.

1.5. 2012 Measurements of CME Faraday Rotation

In this article, we present the results of observations of the radio galaxies 0842+1835, 0843+1547, and 0900+1832, which were occulted by CMEs on 2 August 2012. One of the advantages of using these extragalactic radio sources (relative to spacecraft transmitters and pulsars), which is of importance in our investigation, is that they are extended on the sky and therefore permit simultaneous measurement of Faraday rotation along as many LOS as there are source components with sufficiently large polarized intensities. Obtaining this kind of information from spacecraft transmitters requires simultaneous tracking periods with two separated antennas (see, *e.g.*, Bird, 2007). Another considerable advantage of extragalactic radio sources is that they emit, and are polarized, over a wide range in radio frequency, whereas spacecraft transmitters typically only provide one or two downlink frequencies. Consequently, one can test for the λ^2-dependence of polarization position angle and resolve $n\pi$ ambiguities in the position angle ($n \in \mathbb{Z}$) and ensure that the measured rotations in the position angle are indeed due to Faraday rotation.

There are several reasons why these observations represent a significant improvement and extension of previous CME Faraday-rotation experiments:

i) These observations represent one of the first active hunts for CME Faraday rotation since Bird *et al.* (1985) and this is the first active hunt using the Very Large Array.
ii) While several observations of satellite-downlink signals have been made previously (generally at one frequency along one LOS), these observations represent the first successful attempt to *actively* capture CME Faraday rotation with extragalactic radio sources, which provide multiple LOS over multiple frequencies.

iii) These observations were made with the newly upgraded Very Large Array and consequently provide highly sensitive measurements of CME Faraday rotation.
iv) Both 0842+1835 and 0900+1832 were occulted by one CME and 0843+1547 was occulted by two CMEs (one of which is the same CME that occulted 0842+1835), allowing for a strong test of the efficacy of flux-rope models.
v) Unlike several previous studies (*e.g.* Sakurai and Spangler, 1994a, 1994b; Mancuso and Spangler, 1999, 2000; Spangler, 2005; Ingleby, Spangler, and Whiting, 2007; Kooi *et al.*, 2014), we use simultaneous LASCO-C3 Thomson-scattering data to independently determine the plasma-density structure through the occulting CMEs.
vi) We observed in the B array configuration and are therefore less susceptible to solar interference from the active regions near the solar limb that produced the occulting CMEs as well as the corresponding solar flares.
vii) As a consequence of the previous points, the present observations are the most sensitive to date for our goal of measuring CME Faraday rotation and providing information for the CME plasma structure at heliocentric distances $\approx 10\ R_\odot$.

The organization of this article is as follows: In Section 2 we discuss the source characteristics of radio galaxies 0842+1835, 0843+1547, 0846+1459, and 0900+1832, the geometry of the observations, the method for data reduction, and the imaging and analysis. In Section 3 we discuss the models that we employed for coronal Faraday rotation, Thomson scattering of white light, and flux-rope structure. In Section 4 we present our results for the slow variations in rotation measure associated with the corona alone (0846+1459) and the rotation-measure transients associated with occultation by CMEs (0842+1835, 0843+1547, and 0900+1832) as well as their associated model estimates for the plasma density and magnetic-field structure of the occulting CMEs. In Section 5 we discuss the implications of our measurements and compare our results with the observational results of Bird *et al.* (1985) and modeling results of Liu *et al.* (2007) and Jensen and Russell (2008). Finally, we summarize our results and conclusions in Section 6.

2. Observations and Data Analysis

2.1. Properties of the Target Radio Sources

The basis of this article are radioastronomical observations made in August 2012, during the annual solar occultation of the extragalactic radio sources 0842+1835, 0843+1547, 0846+1459, and 0900+1832, henceforth referred to as 0842, 0843, 0846, and 0900 for the remainder of this article. Images of the polarization structure of these sources made from our VLA observations when the Sun was far from the source (*i.e.* on the reference day, see Section 2.4) are shown in Figure 2, and details of the source characteristics, such as total intensity and linear-polarized intensity (Stokes parameters I and P), are given in Table 1.

The source 0842 is a quasar and appears as a point source at our frequencies of observation. While 0842 does not provide more than one LOS, it is strongly polarized over these frequencies and so provides highly sensitive measurements. The source 0843 is a radio source with two components and consequently provides two closely spaced LOS through the corona: a strong central hot spot, and a weaker northern hot spot (Hot Spots 1 and 2, respectively, in Table 1 and Figure 2). The source 0846 represents a distributed polarized source of radio waves, ideal for probing of the corona with Faraday rotation, (*e.g.* see Figure 2). The polarized emission is strongest in the northern and southern lobe (Hot Spots 1

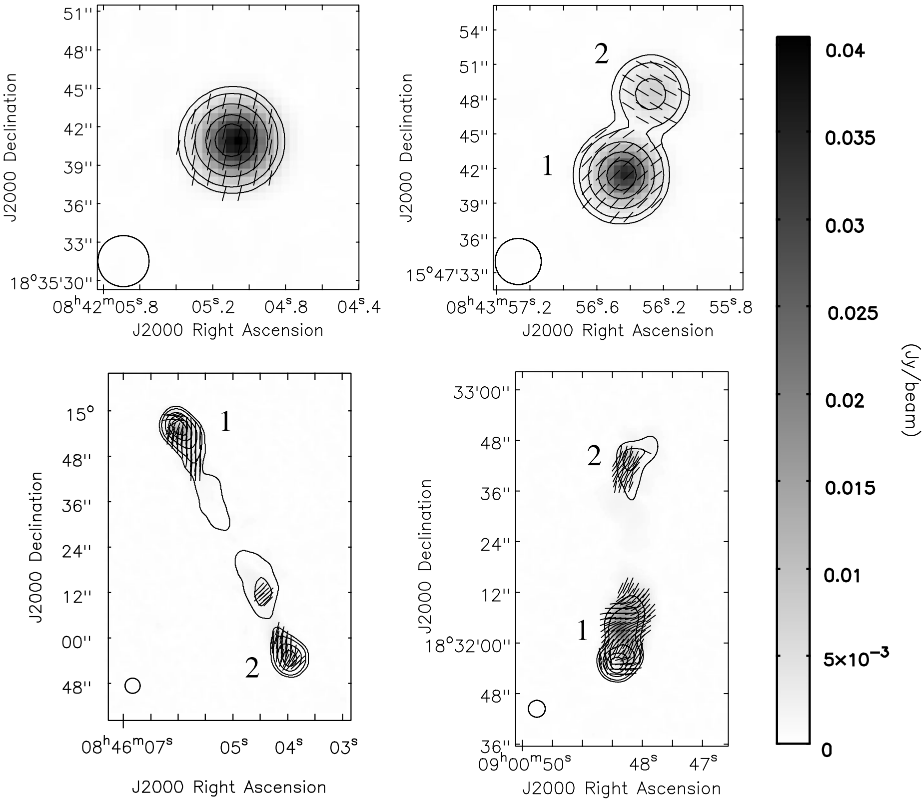

Figure 2 Clean map of the total intensity and polarization structure of the radio sources 0842 (top left), 0843 (top right), 0846 (bottom left), and 0900 (bottom right) on 30 August 2012. These images are a synthesis of the 56 MHz bandpass centered at a frequency of 1.845 GHz. Contours show the distribution of total intensity (Stokes I), and are plotted at −5, 5, 10, 25, 50, and 75% of the peak intensity for each source. The grayscale indicates the magnitude of the polarized intensity (Stokes P). The orientation of the line segments gives the polarization position angle χ. The labels 1 and 2 refer to Hot Spot 1 and Hot Spot 2, respectively, in the analysis presented in this article. The resolution of the image (FWHM diameter of the synthesized beam, plotted in the lower left corner of each image) is four arcseconds. The source structure does not vary significantly over the observed range of frequencies; this is in part because the resolution is fixed across all observing frequencies (see Section 2.5).

and 2, respectively, in Table 1 and Figure 2), with two much weaker components: a northern hotspot at (J2000) RA = $08^{\mathrm{h}}46^{\mathrm{m}}06\overset{\mathrm{s}}{.}1$ and DEC = $14^\circ 59' 58''$, and a southern jet at (J2000) RA = $08^{\mathrm{h}}46^{\mathrm{m}}04\overset{\mathrm{s}}{.}5$ and DEC = $14^\circ 59' 12''$. These two components are too weakly polarized for the analysis presented in this article and are provided here for completeness. The final source for discussion in this article is 0900, and like 0846 it provides multiple LOS through the corona. In this article, we report the results for the strongest hot spots in the southern and northern lobe: Hot Spots 1 and 2, respectively, in Table 1 and Figure 2.

The sources 0843, 0846, and 0900 provide multiple LOS that pass through different parts of the corona and provide information on the spatial inhomogeneity of plasma density and magnetic field. The angular separations between the LOS to the northern and southern hot spots of 0843, 0846, and 0900 are 7.8″, 63.7″, and 42.1″, respectively, corresponding to 5700 km, 46,000 km, and 31,000 km separation, respectively, between the LOS in the

Table 1 Log of observations for August 2012.

Dates of observations		2 Aug 2012	30 Aug 2012
Duration of observing sessions [h]		5.94	3.97
Frequencies of observations [GHz]		1.0 – 2.0	
VLA array configuration		B	
Restoring beam [FWHM][a]		4″[b]	
0842	Range in R_0 [$R_\odot$]	9.6 – 10.6	111.5 – 112.1
	Hot Spot RA, DEC [J2000]	$08^h42^m95\overset{s}{.}1$ $+18°35'41''$	
	I [mJy beam^{-1}][a,c,d]	874 ± 1.9	1070 ± 0.4
	P [mJy beam^{-1}][a,c,d]	33.67 ± 0.92	40.45 ± 0.12
0843	Range in R_0 [$R_\odot$]	9.9 – 10.5	107.5 – 108.1
	Hot Spot 1 RA, DEC [J2000]	$08^h43^m56\overset{s}{.}5$ $+15°47'41''$	
	I [mJy beam^{-1}][a,c,d]	327 ± 0.5	375 ± 0.3
	P [mJy beam^{-1}][a,c,d]	22.42 ± 0.17	25.95 ± 0.12
	Hot Spot 2 RA, DEC [J2000]	$08^h43^m56\overset{s}{.}3$ $+15°47'49''$	
	I [mJy beam^{-1}][a,c,d]	109 ± 0.5	126 ± 0.3
	P [mJy beam^{-1}][a,c,d]	6.20 ± 0.17	7.65 ± 0.12
0846	Range in R_0 [$R_\odot$]	11.1 – 11.4	105.0 – 105.6
	Hot Spot 1 RA, DEC [J2000]	$08^h46^m05\overset{s}{.}9$ $+14°59'54''$	
	I [mJy beam^{-1}][a,c,d]	65 ± 0.5	70 ± 0.5
	P [mJy beam^{-1}][a,c,d]	11.28 ± 0.15	11.92 ± 0.14
	Hot Spot 2 RA, DEC [J2000]	$08^h46^m04\overset{s}{.}0$ $+14°58'57''$	
	I [mJy beam^{-1}][a,c,d]	90 ± 0.5	100 ± 0.5
	P [mJy beam^{-1}][a,c,d]	6.91 ± 0.15	7.40 ± 0.14
0900	Range in R_0 [$R_\odot$]	8.0 – 8.6	95.4 – 96.0
	Hot Spot 1 RA, DEC [J2000]	$09^h00^m48\overset{s}{.}4$ $+18°32'01''$	
	I [mJy beam^{-1}][a,c,d]	57 ± 0.6	67 ± 0.6
	P [mJy beam^{-1}][a,c,d]	14.50 ± 0.23	18.48 ± 0.14
	Hot Spot 2 RA, DEC [J2000]	$09^h00^m48\overset{s}{.}2$ $+18°32'43''$	
	I [mJy beam^{-1}][a,c,d]	28 ± 0.6	36 ± 0.6
	P [mJy beam^{-1}][a,c,d]	5.08 ± 0.23	7.12 ± 0.14

[a]This is for the maps using the data from the entire observation session.

[b]The restoring beam on the day of occultation was fixed to be the same as on the reference day.

[c]Mean and RMS levels for the 1.845 GHz maps (with bandwidth ≈ 56 MHz).

[d]Intensities determined from radio interferometric measurements are typically reported as mJy beam^{-1} because these intensities depend on the synthesized beam solid angle and not just the radio source.

corona. These scale sizes are much larger than the Fresnel scale (60 – 85 km at observational frequencies of 1 – 2 GHz), and therefore these observations are insensitive to irregularities that produce, *e.g.*, intensity scintillations.

The peak intensity of 0846 was $I = 100$ and $I = 90$ mJy beam^{-1} on the reference day and on the day of occultation by the corona, respectively. Similarly, on the day of occultation, the peak polarized intensity decreases from 11.92 to 11.28 mJy beam^{-1}. While the decrease

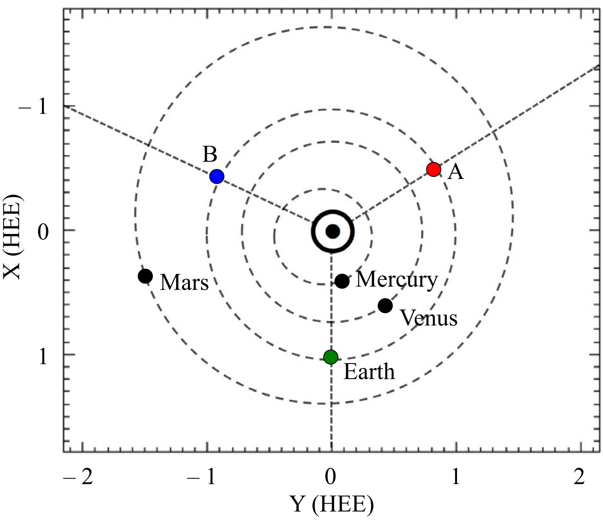

Figure 3 Positions of STEREO-A and STEREO-B relative to the Earth and SOHO at 18:00 UT on 2 August 2012. SOHO is positioned near the Earth (green) at the L_1 point, STEREO-A (red) is located 122° ahead of the Earth, and STEREO-B (blue) is located 115° behind the Earth. The orbits of Mercury, Venus, and Mars are also shown for comparison. The coordinates are Heliocentric Earth Ecliptic (HEE) and given in units of AU. This image was produced using the STEREO orbit tool online at stereo-ssc.nascom.nasa.gov/.

in I and P for 0846 is minor on the day of occultation, there is a considerable decrease in peak I and P for 0842, 0843, and 0900 on the day of occultation. The minor decrease in intensity of 0846 can be attributed to minor angular broadening effects typically associated with small-scale coronal turbulence; however, 0842, 0843, and 0900 were occulted by CMEs (Section 2.3) and so the more substantial decreases in intensities of these three sources is probably due to angular broadening associated with these CMEs. The effects of angular broadening are further discussed in Section 2.5.

2.2. Properties of the Occulting CMEs

Our total intensity white-light analysis in this article relies primarily on coronagraph observations from the SOHO/LASCO-C3 and the STEREO-A and STEREO-B/COR2 instruments. LASCO-C3 has a field of view (FOV) of $3.7-32\ R_\odot$, which overlaps the STEREO-A and STEREO-B/COR2 FOV of $2.5-15\ R_\odot$, respectively. The positions of STEREO-A and STEREO-B relative to the Earth and SOHO on the day of occultation (2 August 2012) are given in Figure 3. SOHO is positioned near the Earth at the L_1 point, and on the day of occultation, STEREO-A was located 122° ahead of the Earth (at a Carrington longitude and heliographic latitude of 284.4° and 0.3°, respectively), and STEREO-B was located 115° behind the Earth (at a Carrington longitude and heliographic latitude of 47.6° and −6.5°, respectively). For comparison, the Carrington longitude and heliographic latitude of the center of the disk was $L0 = 162.4°$ and $B0 = 5.9°$, respectively. Consequently, events appearing on the western limb of the Sun in LASCO-C3 appear just East of disk center in STEREO-A/COR2 and events appearing on the eastern limb of the Sun in LASCO-C3 appear just West of disk center in STEREO-B COR2. For the duration of this article, we refer to the COR2 instrument onboard STEREO-A and STEREO-B as COR2-A and COR2-B, respectively.

Data for all CMEs that occulted our radio sources appear in numerous CME catalogs; Table 2 summarizes these data from three online catalogs: the SOHO LASCO CME Catalog (Gopalswamy *et al.*, 2009), Computer Aided CME Tracking software catalog (CACTus: Robbrecht, Berghmans, and Van der Linden, 2009), and the Solar Eruptive Event Detection System (SEEDS: Olmedo *et al.*, 2008). In this table, the position angle gives the orientation of the erupting CME and is measured counter-clockwise from solar North; the angular width gives the approximate angular size of the CME as measured from the Sun; the linear velocity and acceleration are determined by fitting a first-order and second-order polynomial, respectively, to the height–time measurements for the event.

The first CME, henceforth referred to as CME-1, has the standard three-part structure described in Section 1 and emerged from the southwestern limb of the Sun, entering the COR2-A and LASCO-C3 FOVs at 13:39 UT and 14:06 UT, respectively. The emergence of CME-1 was coincident with the onset of a relatively weak solar flare (GOES Flare Class C1.5) that occurred near solar Active Region (NOAA #) 11529. The flare lasted from 12:10 UT to 13:35 UT and was visible at all wavelengths of the *Extreme-UltraViolet Imager* (EUVI) on STEREO-A. This flare was located at a Carrington longitude and heliographic latitude of 249.5° and $-20°$, respectively, which is within 5° of the coronal magnetic neutral line; consequently, CME-1 originated within close proximity of the coronal magnetic neutral line. This implies that CME-1 initiated near the solar limb on the Earth-side in LASCO-C3 images.

The second CME, henceforth referred to as CME-2, also has the standard three-part structure and erupted from the southwestern limb of the Sun, entering the LASCO-C3 FOV at 15:54 UT. While it appears almost two hours after CME-1 in LASCO-C3, it appears almost immediately after CME-1 in COR2-A, appearing at 13:54 UT. The brightening feature in STEREO-A EUVI images due to the aforementioned C1.5 flare event travels Northwest 20° – 30° toward image center (the far side in LASCO-C3 images), appearing to move along the coronal magnetic neutral line (the position of which was determined using data from the online archive of the Wilcox Solar Observatory [WSO] see Section 3.1.2). This brightening feature, which appeared in close proximity to the initiation point of CME-1 near 12:10 UT, finally disappeared in close proximity to the initiation point of CME-2 near 13:35 UT (as determined by projecting the mean central position angle of the angles provided in column 4 of Table 2 onto the photosphere). Consequently, while CME catalogs such as the SOHO LASCO CME Catalog, CACTus, and SEEDS do not associate this CME with the C1.5 flare event, the location and timing of CME-2 suggest it is coincident with the conclusion of this flare. For these reasons, we conclude that CME-2 erupted from the far side of the Sun, as seen in LASCO-C3 images, near a Carrington longitude and heliographic latitude of $\approx 265°$ and $\approx 0°$, respectively.

The final CME, henceforth referred to as CME-3, emerged from the northeastern limb of the Sun, entering the COR2-B and LASCO-C3 FOVs at 16:09 UT and 16:54 UT, respectively. CME-3 does not have an obvious three-part structure and has more in common with a narrow CME in that it displays a jet-like motion and arises near a preexisting coronal streamer that is adjacent to a coronal dim region in LASCO-C3 images (*e.g.* see Figure 4). This Thomson-scattering dim region may be the consequence of a local coronal hole and therefore may be a region of unipolar flux (*i.e.* open magnetic-field lines). While the magnetic topology that may be inferred from LASCO-C3 images seems ideal for the production of a narrow CME, CME-3 has a larger angular width than typically defines narrow CMEs ($< 10°$, see Chen, 2011), and there were no flare events near the northeastern limb of the Sun near the initiation time. Because of this, we cannot determine the point of eruption in solar coordinates as accurately as for CME-1 and CME-2; however, from the position angles for CME-3 determined from COR2-B and LASCO-C3 images and from the location of the magnetic neutral line, we conclude that CME-3 initiated on the Earth-side of the Sun near a Carrington longitude and heliographic latitude of $\approx 95°$ and $\approx 45°$, respectively. In calculating this, we assume that like CME-1 and CME-2, CME-3 emerged in close proximity to the magnetic neutral line.

Table 2 Occulting CME characteristics on 2 August 2012.

CME identifier	CME catalog	Event time [UT]	Position angle [deg]	Angular width [deg]	Linear velocity [$\mathrm{km\,s^{-1}}$]	Acceleration[a] [$\mathrm{m\,s^{-2}}$]
CME-1	LASCO	13:25	259	108	563	−0.9
	CACTus[b]	13:25	279	140	401	–
	SEEDS[b]	13:25	247	84	491	−0.1
CME-2	LASCO	14:48	286	120	412	−1.5
	CACTus[b,c]	–	–	–	–	–
	SEEDS[b]	15:36	265	92	452	−61.4[d]
CME-3	LASCO	16:36	47	26	649	2.9[e]
	CACTus[b]	16:24	33	36	603	–
	SEEDS[b]	17:00	37	19	562	23.5

[a]The CACTus catalog does not provide acceleration estimates.

[b]Both CACTus and SEEDS have LASCO-based and SECCHI-based catalogs; we report the values from the LASCO-based catalog for direct comparison to the SOHO LASCO CME Catalog.

[c]There is signal confusion in both the LASCO-based and SECCHI-based CACTus catalogs between the CME-1 and CME-2 events because the CMEs overlap.

[d]This value is likely a result of signal confusion between CME-1 and CME-2.

[e]The SOHO LASCO CME Catalog notes that the acceleration is uncertain due to either i) poor height measurement or ii) a small number of height–time measurements.

2.3. Geometry of the Occultation

During the observing session, the orientations of the various LOS to our sources changed relative to the corona. In performing coronal Faraday-rotation observations, the most important parameter describing a given LOS is the heliocentric distance to the proximate point along the LOS, termed the impact parameter [R_0]. The Carrington longitude and heliographic latitude of the proximate point are also important as they are used to determine the location where the LOS crosses the coronal magnetic neutral line [the parameter β_c in Figure 1]. During the 2 August session (details presented in Section 2.4 below), the extended radio source 0846 was only occulted by the corona and was not occulted by a CME (Figure 4); the impact parameter ranged from $11.1-11.4\ \mathrm{R}_\odot$, and there was a corresponding increase in the heliographic latitude of the proximate point from -70.4° to -66.4° and increase in the Carrington longitude from 224.0° to 225.9°.

The radio source 0843 was slightly closer to the Sun on the day of occultation, with a range in impact parameters of $9.9-10.5\ \mathrm{R}_\odot$ corresponding to an increase in the heliographic latitude of the proximate point from -50.3° to -46.6° and decrease in the Carrington longitude from 240.2° to 238.0°. As may be seen in Figure 4, the LOS to 0843 primarily sampled a coronal dim region before occultation; such regions may be associated with a coronal hole, where magnetic-field lines are thought to be nearly unipolar and radial.

Source 0843 was occulted by two CMEs on 2 August 2012: the first, CME-1, began occulting the LOS to this source just after 15:42 UT, and the second, CME-2, began occultation at 18:30 UT. By 20:06 UT, CME-1 passed beyond the LOS to 0843; however, CME-2 continued to occult this source until the end of the session. Figure 4 demonstrates the sequence of these events, as projected from three dimensions onto the two-dimensional LASCO-C3

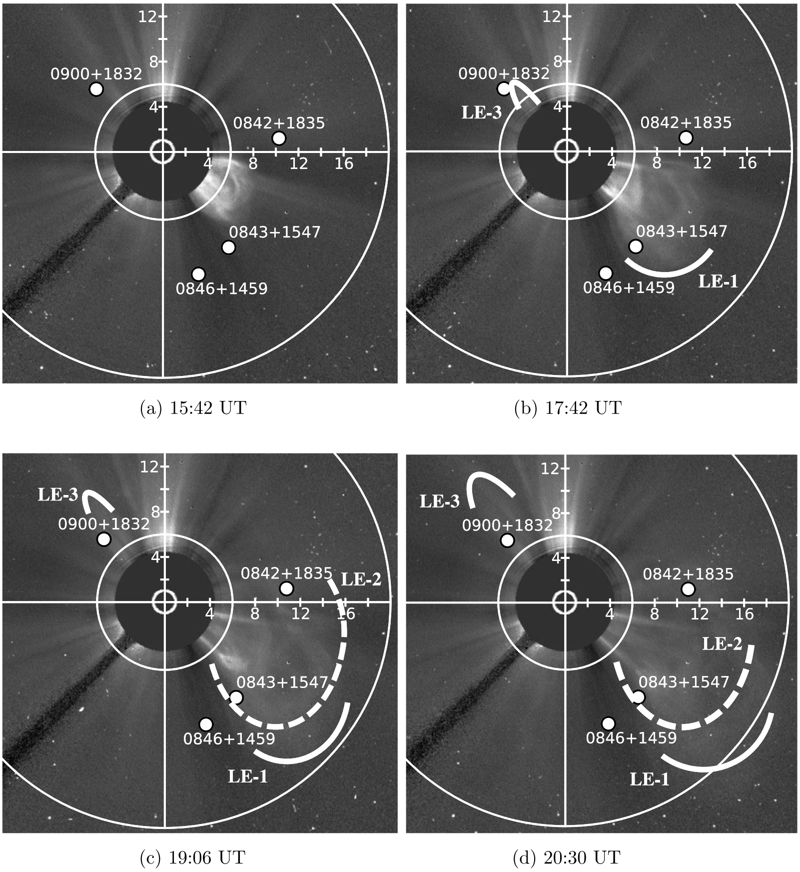

Figure 4 Corona and CMEs on 2 August 2012 as observed with the LASCO-C3 coronagraph. White plotted points are the LOS to the radio sources (a) just before occultation; (b) during occultation of 0842, 0843, and 0900 by CME-1, CME-2, and CME-3, respectively; (c) during occultation of 0843 by both CME-1 and CME-2; and (d) during occultation of 0843 by CME-2 only. 0846 was not occulted by a CME. The solid curves (LE-1 and LE-3) and dashed curves (LE-2) represent the leading edges of CMEs originating on the Earth side and far side of the Sun, respectively. These figures are projections of the three-dimensional LOS and CME geometries onto the two-dimensional LASCO-C3 images and correspond to the left column (LASCO-C3 vantage point) in Figure 5. The photosphere appears as the white circle centered inside the dark occulting disk, and the horizontal axis is the heliographic Equator with scale given in $R_\odot$. Images are from the LASCO public archive: sohowww.nascom.nasa.gov.

images. Because CME-1 and CME-2 overlap, we have outlined the leading edges of their bright outer loops (LE-1 and LE-2, respectively) in this figure. From the vantage point of LASCO-C3, CME-1 is in the foreground, and the leading edge, LE-1, is denoted by a solid line in Figure 4. CME-2 is in the background, and the leading edge, LE-2, is denoted by a dashed line.

The quasar 0842 had the largest range in impact parameters (9.6 – 10.6 $R_\odot$) because the LOS was located near the heliographic Equator; the heliographic latitude of the proximate point decreased from 11.8° to 11.2° and the Carrington longitude decreased from 251.0° to 247.4°. As may be seen in Figure 4, 0842 was occulted by CME-2 beginning near 16:30 UT and continued to be occulted by this CME for the duration of observations.

The radio galaxy 0900 had the smallest impact parameters, ranging from 8.6 $R_\odot$ at the beginning of the session to 8.0 $R_\odot$ at the end, corresponding to an increase in the heliographic latitude of the proximate point from 38.0° to 42.7° and a decrease in the Carrington longitude from 72.3° to 68.1°. At the beginning of the observations, 0900 was occulted by a coronal streamer, and at 17:18 UT, the narrow jet-like CME-3 began occulting this source and continued to do so for the remainder of the observing session.

2.4. Observations and Data Reduction

All radio observations were performed using the Karl G. Jansky Very Large Array (VLA) of the National Radio Astronomy Observatory (NRAO)[1], and all data reduction was performed with the Common Astronomy Software Applications (CASA) data-reduction package (McMullin *et al.*, 2007). Because CMEs cannot currently be predicted with any precision, we had to make special arrangements with the staff at NRAO to schedule observations: we prepared a set of scheduling blocks for every day in the Summer of 2012 (22 June – 20 August).

We selected a constellation of radio sources from the NRAO VLA Sky Survey (NVSS: Condon *et al.*, 1998) that would be occulted by the solar corona for each potential observation day. We chose sources based on three primary criteria:

i) proximity to the Sun (5 – 15 $R_\odot$)
ii) degree of linear polarization ($P > 5$ mJy beam^{-1})
iii) a requirement of eight or nine of the strongest polarized sources evenly distributed around the Sun.

Because we would be observing at low frequencies (1.0 – 2.0 GHz), the Sun ($\approx$1 MJy at 10 GHz) enters the side lobes of the observing antennas at small impact parameters, increasing the noise in the signal considerably and preventing sensitive measurements typically <5 $R_\odot$. Beyond 15 $R_\odot$, coronal contributions to Faraday rotation are minimal and typically comparable in magnitude to ionospheric Faraday rotation. Consequently, we chose sources within the range 5 – 15 $R_\odot$ where we were confident that we could make sensitive measurements of CME-induced Faraday rotation. Regarding the last point, we chose sources that were scattered around the Sun instead of a set of sources grouped in one region (*e.g.* aligned with an active region) because of the unpredictable nature of CMEs. Having sources scattered around the Sun provides a better chance of measuring Faraday rotation through a CME, even if the CME only occults one or two sources.

We closely monitored the Sun during these days and would submit a set of observations 24 hours in advance of the day on which we wished to observe. We chose an observation day based on the following criteria:

i) multiple active regions were within 20° of the solar limb
ii) no major flare or CME events associated with these active regions in the previous 48 hours
iii) increases in size of sunspots or sunspot groups associated with these active regions in the previous 48 hours
iv) brightening in EUV images of these active regions, as this may be associated with strengthening magnetic fields in the previous 48 hours.

[1] The Karl G. Jansky Very Large Array is an instrument of the National Radio Astronomy Observatory. The National Radio Astronomy Observatory is a facility of the National Science Foundation operated under cooperative agreement by Associated Universities, Inc.

The first criterion increases the likelihood of capturing a CME demonstrating the traditional three-part structure in LASCO-C3 images. The second criterion increases the likelihood of a large CME event because the solar active regions have not been releasing stored energy in recent CME events. The other two criteria increase the probability of a CME erupting on the day of observation. Based on these criteria, we made three sets of six-hour observations (2 August, 5 August, and 19 August) when sources were near the Sun, and one set of four-hour reference observations (30 August) when all three sets of sources were distant from the Sun, allowing for measurement of the sources' intrinsic polarization properties, unmodified by the corona. We were successful in capturing a CME on 2 August. Observations of the CME-occulted target sources performed on 2 August 2012 lasted from 14:46 to 20:53 UT, and the reference observations performed on 30 August 2012 lasted from 15:04 to 19:03 UT. While CMEs did erupt on 5 August and 19 August, these CMEs did not emerge during the period of our observations on those days.

In this article, we discuss the Faraday rotation to the three sources occulted by CMEs (0842, 0843, and 0900) as well as one source occulted only by the corona (0846) for comparison. The details of these observations and resultant data are given in Table 1. Even though the other five sources from 2 August and the target sources from 5 and 19 August were not occulted by CMEs, these sources sample different regions of the corona – with proximate points located at a range of heliographic latitudes and longitudes – and provide further information on the global plasma structure of the corona at $5-15\ R_{\odot}$. Analysis and discussion of these data will appear in another article in preparation.

The observations were similar in nature to those previously reported by Sakurai and Spangler (1994a), Mancuso and Spangler (1999, 2000), and Kooi *et al.* (2014), and described in those articles. The main features of the observations are briefly summarized below. We also indicate features of the 2012 observations that differ from those of our previous investigations.

i) Observations were made in the B-array configuration. This is important because we were purposely observing near strong solar active regions at the solar limb, which produce strong solar interference (*i.e.* strong uneditable fringes due to active regions on the Sun) on short baselines. The VLA has four standard array configurations: A, B, C, and D, with maximum baselines (*i.e.* maximum distances between any two dishes) of ≈ 1, 3.4, 11.1, and 36.4 km, respectively. Consequently, the A- and B-array configurations have very few short baselines, and therefore the data are less affected by solar interference; however, the shortest interferometer baselines[2] (≤ 4 kλ) still had to be discarded[3]. This was done for all sources and for both sessions in order to allow more direct comparison between the reference day and the day of occultation.
ii) We used an integration time of 15 seconds, which in the B configuration corresponds to an acceptable $\approx 5\%$ time-averaging loss in signal amplitude[4].
iii) Simultaneous observations were made at (L-band) frequencies of 1.0 – 2.0 GHz divided into 16 bands, each with a resolution (channel width) of 1 MHz.
iv) Owing to radio-frequency interference (RFI), large segments of the bandwidth had to be excised. Of the original 16 frequency bands, we retained 7 with center frequencies of 1.356 GHz (bandwidth = 34 MHz), 1.409 (bandwidth = 56 MHz), 1.473

[2] 0.21 km (or 1.3 kλ at 1.845 GHz) is the smallest baseline available in B configuration.

[3] In more compact array configurations, this restriction would represent a significant loss of data, *e.g.* the maximum UV distance at 1.845 GHz in the C and D configurations is 21 kλ and 6.2 kλ, respectively, compared to 68 kλ in B configuration.

[4] See the Observational Status Summary documentation for the VLA at science.nrao.edu/facilities/vla/docs

(bandwidth = 56 MHz), 1.725 (bandwidth = 40 MHz), 1.781 (bandwidth = 56 MHz), 1.845 (bandwidth = 56 MHz), and 1.899 (bandwidth = 37 MHz). Note that the first three bands, and similarly, the other four bands, are not contiguous; the edge channels of each band were removed.

v) Observations of the target sources were made in scans of three to four minutes in duration; the time-on-source for a given scan depended on the magnitude of the polarized intensity $[P]$ given in the NVSS catalog. Each set of target scans was bracketed by 1.3-minute observations of a phase calibrator, for a total of ten scans on the day of occultation. The average interval between each scan was ≈ 32 minutes.

vi) The main calibrator for both sessions was J0825+0309. This source was used for phase and amplitude calibration, as well as measurement of instrumental polarization. In previous observations (*e.g.* Kooi *et al.*, 2014), we would observe a second calibrator source as an independent check of the polarimeter calibration. We have always found that the polarization-calibration values for both the primary phase calibrator and secondary phase calibrator were in excellent agreement; therefore, we did not include a second phase calibrator for these observations, choosing instead to maximize the time on our target sources. The range in angular separation between this phase calibrator and the target sources was $12.8^\circ - 17.6^\circ$. These values are higher than typical VLA phase calibrator–target source separations ($\leq 10^\circ$) because the phase calibrator needs to be far enough from the Sun to remove the possibility for the coronal plasma to influence this source. On the day of occultation, the impact parameter for J0825+0309 was $R_0 \approx 60$; consequently, coronal influence on the calibration scans is negligible. Furthermore, previous investigations (*e.g.* Ingleby, Spangler, and Whiting, 2007) performed sensitive Faraday rotation experiments with separations $\lesssim 15^\circ$, and so our phase calibrator–target source separations are acceptable.

vii) Polarization data were corrected for estimated ionospheric Faraday rotation using the Common Astronomy Software Applications (CASA) task *gencal* specifying the option caltype = tecim. Before version 4.3.0, CASA did not have the ability to mitigate ionospheric Faraday rotation; however, George Moellenbrock (NRAO) and Jason Kooi implemented ionospheric Faraday-rotation corrections in CASA version 4.3.0, and these corrections appear in all later versions (see Kooi, 2016). The algorithm is similar to the Astronomical Image Processing System (AIPS) program procedure VLBATECR and functions by retrieving ionosphere model data from the Crustal Dynamics Data Information System (CDDIS), producing a CASA image file of the global vertical total electron content (VTEC) values, and generates corrections for the ionospheric Faraday rotation based on these VTEC values. Estimates for the ionospheric Faraday rotation measure ranged from $2.8 - 3.7\ \mathrm{rad\,m^{-2}}$ on 2 August and about $2.6 - 3.6\ \mathrm{rad\,m^{-2}}$ on 30 August for the four target sources. The ionospheric Faraday rotation is similar for all target sources because they are within 5° of each other; furthermore, we observed at similar local sidereal times (LST) on both days. Because of the method used to determine the coronal Faraday rotation (see Section 2.5), the total contribution from any residual ionospheric Faraday rotation should be negligible ($\leq 0.1\ \mathrm{rad\,m^{-2}}$).

viii) The instrumental polarization, described by the antenna-specific D factors (Bignell, 1982; Sakurai and Spangler, 1994b), was determined from the observations of J0825+0309 in both sessions. Even though we could not use the same reference antenna in both sessions, the amplitudes and phases of the D factors were nearly identical for all antennas for both sessions. In addition, the amplitudes of the D factors are higher for the upgraded VLA antennas, $D \approx 5 - 10\%$, than for the pre-upgrade antennas, $D \approx 1 - 4\%$, studied by Sakurai and Spangler (1994b). These results are similar to those given by Kooi *et al.* (2014).

ix) The net RL phase difference was determined using observations of 3C 286. To test the precision of these calibration solutions, a second calibrator with known polarization, 3C 138, was calibrated using the RL phase difference solutions from 3C 286; the measured position angle was within 0.3° of the values listed in VLA calibrator catalogs for both sessions and all observing frequencies.

x) Of the 27 antennas used during these observations, three had to be excised on the reference day: two had abnormally high D-factors ($\approx 50\%$), and one antenna's L-band receiver had been removed, and it therefore provided no data. On the day of occultation, only one antenna had to be removed because its cross-hand (RL and LR) phases were poor after calibration.

2.5. Imaging with VLA Radio Data

For each source, we generated maps in the Stokes parameters I, Q, U, and V for each scan as well as a "session map" made from all of the data on a given day, at a given frequency. The session maps provide a measure of the mean Faraday rotation over the entire observing session; the individual scan maps, however, allow for examination of the temporal variations over the observing session, with a resolution on the order of the interval between scans: ≈ 32 minutes.

The imaging process was similar to the method described by Kooi *et al.* (2014); consequently, we indicate here only features that differ from the results of Kooi *et al.* (2014):

i) The calibrated VLA visibility data were split into the seven bandpasses given in Section 2.4 with center frequencies of 1.356 GHz (bandwidth = 34 MHz), 1.409 (bandwidth = 56 MHz), 1.473 (bandwidth = 56 MHz), 1.725 (bandwidth = 40 MHz), 1.781 (bandwidth = 56 MHz), 1.845 (bandwidth = 56 MHz), and 1.899 (bandwidth = 37 MHz).

ii) Each bandpass was averaged in frequency from 1 MHz channel widths (resolution) to 4 MHz in order to expedite mapping. We did not average over the whole bandpass because that would introduce significant bandwidth-smearing effects.

iii) We used the CASA task clean using the multifrequency synthesis mode with a cell size of 0.6″ to generate the maps.

iv) We generated maps using a natural weighting scheme because we are primarily concerned with sensitivity and not resolution.

v) To accurately compare the maps restored at each of the seven frequencies, the maps produced from observations on the day of occultation were restored using the same beam size (4.0″, the beam size for the lowest frequency bandpass) as maps from the reference observations on 30 August; furthermore, this same beam size was used to restore the maps at all frequencies.

vi) One iteration of phase-only self-calibration was performed, which improved the ratio of peak intensity to the RMS noise (termed the dynamic range) by factors of 2 – 4, depending on the bandpass.

vii) We generated maps of the (linear) polarized intensity [P] and the polarization position angle [χ] directly from the maps of Stokes Q and U according to $P = \sqrt{Q^2 + U^2}$ and $\chi = 0.5 \arctan(U/Q)$.

viii) We examined the session maps for local maxima in polarization intensity (typically $P > 5$ mJy beam^{-1}) for each source on the reference day. We chose these locations in order to maximize the sensitivity of our measurements because the error in measuring the polarization position angle is $\approx \sigma_P / 2P$, where σ_P is the error in measuring P; consequently, stronger P provides a more robust measurement for χ. We then measured the values of the polarization quantities I, Q, and U for the pixel with peak P and derived the polarization quantities P and χ for the individual scan and session maps on both observation days.

ix) Of the extended sources, the polarized intensity of both the north and south hot spots of 0843 are strong enough to allow accurate polarization measurements; however, the value of P was too low to allow accurate measurements over most of the extended emission in 0846 and 0900. In the rest of the article, the analysis is based on measurements for the hot spot in the northern and southern lobes where the polarized intensity was at a local maximum in the session map for the reference day, providing two LOS for both sources. While the local maxima in P were collocated with the local maxima in I for 0842 and 0843, the local maxima in P were offset from the local maxima in I for 0846 and 0900 by $\lesssim 4''$ and $\lesssim 7''$, respectively.

x) We calculated the coronal Faraday rotation $[\Delta\chi^i(\nu; x, y)]$ for the ith scan map at frequency ν by straight subtraction:

$$\Delta\chi^i(\nu; x, y) = \chi^i_{\text{occ}}(\nu; x, y) - \chi_{\text{ref}}(\nu; x, y) \tag{3}$$

for $i \in [1, 10]$, where $\chi^i_{\text{occ}}(\nu; x, y)$ are the polarization position angles at frequency ν and at location (x, y) for the ith scan map on the day of occultation, and $\chi_{\text{ref}}(\nu; x, y)$ is the polarization position angle for the same frequency and location on the session map for reference observations. This subtraction method eliminates Faraday rotation caused by the background interstellar medium and typically reduces the effects of polarimeter calibration error, which would otherwise require second-order instrumental polarization calibration (*e.g.* see Sakurai and Spangler, 1994b).

xi) We then used a least-squares algorithm to determine the rotation measure [RM] for each individual scan from the $\Delta\chi$ for each of the seven bandpasses. The fit is weighted by the radiometer noise because the fidelity of the data for the bandpasses centered at frequencies 1.409, 1.473, 1.781, and 1.845 GHz was superior to the other three bandpasses.

Similar to Kooi *et al.* (2014), these maps demonstrate a lack of visible angular broadening of the radio sources; however, there is a measurable decrease in I and P on the day of occultation, particularly for the three sources occulted by CMEs. In radioastronomical observations, the measured intensity is the convolution of the true intensity with a point-spread function. In these coronal observations, the point-spread function for the target sources is the convolution of the synthesized beam with the power pattern of the angular broadening. Following the procedure outlined by Kooi *et al.* (2014), we determined the Gaussian equivalent angular broadening disk and the corresponding drop in intensity for each target source.

The angular broadening disk for the source that was occulted only by the corona, 0846, was asymmetric, but small ($1.4'' \times 0.5''$), and corresponds to a drop in intensity of 4 – 7%. This is consistent with the decrease of 10% and 5% in I and P, respectively, in Hot Spot 1. The sources occulted by CMEs had more pronounced angular broadening associated with them: the angular broadening disks for the extended sources, 0843 and 0900, were $1.6'' \times 0.8''$ and $3.4'' \times 1.9''$, respectively, corresponding to drops in intensity of 6 – 12% and 13 – 16%, respectively. Again, these are consistent with the decreases in peak I and P shown in Table 1 for these sources. For 0842, the measured angular broadening disk is $1.0'' \times 0.5''$, corresponding to a decrease in intensity of 4%. This is considerably less than the measured 18% decrease for this source; however, it is difficult to measure angular broadening in 0842 because it is a point source and we have specified the restoring beam size. Finally, as further evidence, the phase calibrator was sufficiently far from coronal influences, there was no evidence of angular broadening for the phase calibrator.

The small size of the Gaussian disks for the target sources is also consistent with the lack of visible broadening in the maps. Because the broadening is not significant and is, in fact, smaller than the minimal effect measured by Kooi *et al.* (2014), we did not correct for this phenomenon (*e.g.* by convolving the session maps on the reference day with Gaussian equivalent disks).

2.6. Imaging with LASCO-C3 White-Light Data

As discussed in Section 1.2, observations of the corona are primarily obtained using white-light coronagraphs (*e.g.* LASCO-C3, COR2-A, and COR2-B), which observe radiation from the photosphere that has been Thomson-scattered by electrons in the coronal plasma. In order to derive independent estimates for the plasma density, we use white-light images from the LASCO-C3 instrument. LASCO-C3 is ideal because SOHO is aligned with the Earth, and therefore, the LOS from a given radio source to the VLA in our radioastronomical data is similar to the LOS from that source to LASCO-C3 in optical white-light data.

Here, we outline the basic procedure that we employed to produce LASCO-C3 images suitable for determining Thomson-scattering brightness profiles for the LOS to each of our target sources:

i) We downloaded all LASCO-C3 Level 1 FITS images for 2 August as well as for the 15 days before 2 August and the 15 days following 2 August, for a total of 31 days. The Level 1 FITS images are scaled to the mean solar brightness [$B_\odot$] and have been preprocessed to correct for the flat-field response of the detector, radiometric sensitivity, stray light, geometric distortion, and vignetting. These images are made available to the public by the Naval Research Laboratory (NRL) at lasco-www.nrl.navy.mil.

ii) For each of the 31 days, we made a pixel-by-pixel median image. By determining the median value pixel-by-pixel instead of image-by-image, transients such as background stars, CMEs, and comets are removed. We chose to make a pixel-by-pixel median image over a simpler pixel-by-pixel minimum image because a daily median image is less susceptible to particularly low brightness values such as may be associated with a data gap due to interference or preprocessing issues.

iii) We then produced the pixel-by-pixel minimum image for this 31-day period. This final median-minimum image contained no signs of background stars, fast transients such as CMEs or comets, or slow transient structures such as coronal streamers; the final median-minimum image instead appears as a hazy elliptical disk such as may be associated with the F-corona.

iv) We subtracted the median-minimum image for the 31-day period from all LASCO-C3 Level 1 FITS images on 2 August, the day of occultation. The Thomson-scattering brightness varies between 10^{-12} – 10^{-11} $B_\odot$ at heliocentric distances relevant to our radio observations (8.0 – 11.4 $R_\odot$), which is consistent with model K-corona brightness curves (*e.g.* as presented in Saito, Poland, and Munro, 1977; Hayes, Vourlidas, and Howard, 2001).

v) We developed Python code to determine the LOS pixel position to all target sources in each LASCO-C3 subtraction image on the day of occultation. The Thomson-scattering brightness scaled to the mean solar brightness [$B_T/B_\odot$] for each LOS was then given by the pixel value at this position. Doing this for all LASCO-C3 subtraction images produces a Thomson-scattering brightness time series for each target source with a time resolution of 12 minutes, the time interval between each LASCO-C3 image. We only measure the Thomson brightness along one LOS (to the target source center) even for the extended sources because the spatial resolution of the LASCO-C3 images is considerably lower (1 pixel ≈ 0.06 $R_\odot \approx 56.0''$) than our radioastronomical observations ($4.0''$).

vi) To estimate the error in $B_T/B_\odot$, we calculated the mean value for $B_T/B_\odot$ in the outer FOV of the LASCO-C3 subtraction images (heliocentric distances of $25-30$ $R_\odot$), the region that is expected to be noise-dominated. For all images, this value was within the range $0.2-0.5 \times 10^{-12}$.

There are two issues that are important to consider in performing this median-minimum subtraction method. First is the possibility that this method will not only remove the F-corona, but will oversubtract and remove a portion of the K-corona contribution. This is especially true if the K-corona is quasi-static, as is often the case during solar minimum conditions. Our observations in 2012 were made during solar maximum, and therefore the corona was very dynamic. Over the 31 days used to produce the median-minimum F-corona image, even large-scale quasi-static structures such as helmet streamers typically lasted fewer than $\lesssim 5$ days. Finally, we observed at heliocentric distances of $8.0-11.4$ $R_\odot$; oversubtraction of the K-corona is more pronounced at shorter distances. For these reasons, it is unlikely that the Thomson-scattering brightness time series for our target sources sample regions where the K-corona is significantly oversubtracted. The second consideration is whether the observations are noise-dominated. Our Faraday-rotation observations were already limited to < 20 $R_\odot$ because coronal Faraday rotation is negligible beyond this distance; consequently, our LOS are far from the outer FOV where the brightness is expected to be noise-dominated.

The LASCO-C3 images also provide us with the unique ability to track the progression of the LOS for a given target source through the CMEs observed on August 2 (*e.g.* Figure 4). We measured the span in pixels to which each LOS penetrated a CME for every LASCO-C3 image. This CME penetration length [y_p] was used in modeling the Thomson brightness and Faraday rotation associated with occultation by a CME and is illustrated in Figure 6. For CMEs displaying the classical three-part structure (*e.g.* CME-1 and CME-2), the radius of the CME [R_CME] was also determined using these images. For the analysis that follows, it is important to emphasize that in measuring R_CME, we assumed that the flux rope consists of both the inner cavity and the outer loop (*i.e.* we associate the leading edge of the outer loop with the boundary of the flux rope) and the flux rope does not include the bright core. This distinction is important because some CME models assume a sheath region in the outer loop, and therefore only the inner cavity is associated with the magnetic flux rope.

Measuring y_p and R_CME for the LOS to 0843 required additional information because it was occulted by both CME-1 and CME-2 from 18:30 UT to 20:06 UT. To pinpoint the time at which 0843 was occulted by CME-2 and the time at which occultation by CME-1 ended, as well as to track the leading edges of CME-1 and CME-2 (LE-1 and LE-2, respectively), we relied on the additional vantage point provided by COR2-A. Figure 5 gives an illustration of the LASCO-C3 and COR2-A vantage points as well as a top-down view of the Sun–LOS plane. The LASCO-C3 vantage point (left column) is similar to Figure 4 with CME-1 (red) and CME-3 (green) appearing in the foreground and CME-2 (blue) appearing in the background. The geometry of SOHO and STEREO-A on the day of occultation is demonstrated in the right column of Figure 5, and as a consequence of this geometry, CME-1 and CME-3 appear in the background of the illustration of the COR2-A vantage point (middle column) and CME-2 appears in the foreground. The rows demonstrate the progression of CME-1 (red) and CME-2 (blue) as they occult 0843 during the observing session, as well as the progression of CME-3 (green), which only occults the LOS to 0900.

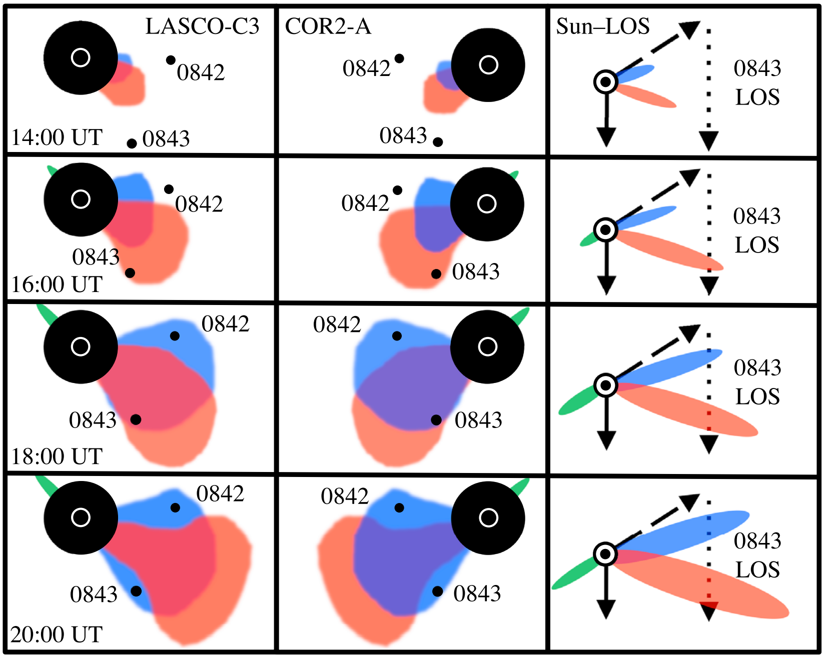

Figure 5 Illustration of the LASCO-C3 (left column) and COR2-A (middle column) vantage points as well as a top-down view of the Sun–LOS plane (right column). The rows demonstrate the progression of CME-1 (red) and CME-2 (blue) before they occult 0843 near 14:00 UT (top row), during occultation by CME-1 alone near 16:00 UT (second row), during occultation by both CME-1 and CME-2 near 18:00 UT (third row), and during occultation by CME-2 alone near 20:00 UT (bottom row). The progression of CME-3 (green) is also shown; however, it does not occult 0843. In the LASCO-C3 and COR2-A columns, the photosphere appears as the white circle centered inside the dark occulting disk, 0842 and 0843 appear as the black plotted points labeled "0842" and "0843", respectively, and the horizontal axis is the heliographic equator. In the top–down view of the Sun–LOS plane for 0843, the solid arrow is directed toward LASCO-C3, the dashed arrow is directed toward COR2-A, and the dotted arrow gives the LOS to 0843.

Tracing the approximate position of the LOS to 0843 onto COR2-A images (downloaded from secchi.nrl.navy.mil) made it possible to follow the progression of this LOS through CME-1 (appearing in the foreground of LASCO-C3 images and the background of COR2-A images) and CME-2 (appearing in the background of LASCO-C3 images and the foreground of COR2-A images). Difference images (*i.e.* images produced by taking the pixel-by-pixel difference between the ith image and the $(i+1)$ image) for both LASCO-C3 and COR2-A were also used to more accurately track the leading edges LE-1 and LE-2. It is worth noting that inclusion of this second CME is not merely adding more fit parameters, it is *required* by the independent STEREO-A data. It is also important to emphasize that we could *not* perform the analysis that follows for 0843 without the multiple vantage points provided by the SOHO and STEREO-A spacecraft, as illustrated in Figure 5.

3. Coronal and CME Models

To obtain information on the plasma structure from Thomson scattering [Equation (2)] and Faraday rotation [Equation (1)], we employ simplified analytic expressions for the plasma density and magnetic field. We begin by first modeling the background coronal plasma; our ability to estimate the background corona is important for correctly interpreting the CME data. We then employ flux-rope models to reproduce observations of CME-1, CME-2, and CME-3.

3.1. Modeling the Background Corona

3.1.1. Model for Coronal Thomson Scattering

In our model for the background coronal plasma, we assume that the plasma density depends only on the heliocentric distance [r]. To model the coronal Thomson-scattering brightness [B_T], we must determine the form of the geometric function $\mathcal{G}(\boldsymbol{r})$ in Equation (2). As discussed in Section 1.2, $\mathcal{G}(\boldsymbol{r})$ depends on assumptions about solar limb darkening and heliocentric distance. For spherically symmetric plasma: $\mathcal{G}(\boldsymbol{r}) = \mathcal{G}(r)$. The full form of $\mathcal{G}(r)$ (given as Equation (17) by van de Hulst, 1950) is

$$\mathcal{G}(r) = \left(\frac{3}{4}\sigma_T \mathrm{R}_\odot \mathrm{B}_\odot\right)\left[\left(2 - \frac{R_0^2}{r^2}\right)\mathcal{A}(r) + \frac{R_0^2}{r^2}\mathcal{B}(r)\right]\frac{r}{\sqrt{r^2 - R_0^2}}, \tag{4}$$

where σ_T, $\mathrm{R}_\odot$, and $\mathrm{B}_\odot$, are the Thomson-scattering cross-section, solar radius, and mean surface brightness of the Sun. The heliocentric distance to a given point along the LOS at which scattering occurs is r, and R_0 is the impact parameter for the LOS, both given here in units of $\mathrm{R}_\odot$. $\mathcal{A}(r)$ and $\mathcal{B}(r)$ are geometric factors such that $\mathcal{A}(r)$ is the fraction of $2\mathcal{A}(r) + \mathcal{B}(r)$ that is proportional to the mean square of the electric-field-vector components in any transversal direction, and $\mathcal{B}(r)$ is the fraction of $2\mathcal{A}(r) + \mathcal{B}(r)$ that is proportional to the mean square of the vector components in the radial direction. The functional forms of $\mathcal{A}(r)$ and $\mathcal{B}(r)$ and the geometry involved in coronal Thomson scattering are given by van de Hulst (1950) and are not repeated here.

We treat the Sun as a point source in Equation (4). In this limit, $\mathcal{A}(r) \to 1/2r^{-2}$ and $\mathcal{B}(r) \to 0$. As demonstrated by van de Hulst (1950), $\mathcal{A}(r)$ and $\mathcal{B}(r)$ rapidly approach these limits, reaching them by heliocentric distances of $5\mathrm{R}_\odot$. We are interested in Thomson scattering at impact parameters $\geq 8\mathrm{R}_\odot$ (see Table 1); consequently, this assumption is valid for our purposes. Applying this assumption and redefining Equations (2) and (4) in terms of the β-angle defined in Figure 1 gives the form

$$\mathrm{B_T}/\mathrm{B}_\odot = \left(\frac{3\sigma_T \mathrm{R}_\odot}{16 R_0}\right)\int_{-\pi/2}^{\pi/2}\left[1 + \sin^2(\beta)\right] n_\mathrm{e}(R_0, \beta)\,\mathrm{d}\beta. \tag{5}$$

The specific form for the plasma density we choose is a single power-law representation:

$$n_\mathrm{e}(r) = N_0 r^{-\alpha}, \tag{6}$$

where N_0 and α are free parameters and r is in units of $\mathrm{R}_\odot$. The resulting expression for Thomson scattering is then

$$\mathrm{B_T}/\mathrm{B}_\odot = \left(\frac{3\sigma_T \mathrm{R}_\odot N_0}{8}\right) R_0^{-\alpha-1}\left(\frac{\sqrt{\pi}}{1+\alpha}\right)\frac{\Gamma(\frac{5}{2} + \frac{\alpha}{2})}{\Gamma(2 + \frac{\alpha}{2})}. \tag{7}$$

In particular, we use the same model value $\alpha = 2.36$ as Kooi *et al.* (2014). This power law gives predictions that have been in fairly good agreement with measurements reported by Sakurai and Spangler (1994a), Spangler (2005), and Ingleby, Spangler, and Whiting (2007). While there have been a number of alternative power laws presented over the years (*e.g.*

Table 3 Model parameters for the background coronal plasma.

Source	$\beta_{c,1}$	$\beta_{c,2}$ [a]	N_0 [b] [10^5 cm^{-3}]	n_e ($r = 1$ AU) [c] [cm^{-3}]	B_0 [d] [G]
0842	[$-22.4°$, $-25.4°$]	–	3.05 ± 0.25	2.8	1.01
0843	[$19.0°$, $21.3°$]	–	2.19 ± 0.26	2.1	1.01
0846	[$21.7°$, $22.8°$]	–	3.10 ± 0.47	2.9	1.01
0900	[$30.4°$, $30.8°$]	[$-44.2°$, $-52.4°$]	4.20 ± 0.58	4.0	1.01

[a] Only 0900 was occulted by two neutral lines.

[b] Determined from a least-squares fit to the Thomson-scattering brightness attributed to the background corona.

[c] Determined by assuming Equation (6) holds out to 10 $R_\odot$, then extrapolating out to 1 AU with $n_e(r) \propto r^{-2}$.

[d] Value taken from Sakurai and Spangler (1994a).

$N_0 = 1.61 \times 10^6$ cm^{-3} and $\alpha = 2.45$ in Pätzold *et al.*, 1987), the exact form of the power laws assumed in Equation (6) should not be crucial for the results presented here for two reasons. First, the different functional forms give very similar values at heliocentric distances characteristic of our observations, and second, our observations were made in a narrow range of impact parameters ($8 - 11.4$ $R_\odot$).

We specify α and determine N_0 by fitting Equation (7) to the Thomson-scattering profile for a given source using a least-squares method. For 0846, we fit to the B_T data over the entire observing period because the source was not occulted by a CME. For sources occulted by a CME during radio observations, we fit to the B_T data for the three hours before occultation by the leading edge of the CME. The values of N_0 determined from each fit for a given LOS are shown in Table 3 and the corresponding B_T curve for the background coronal plasma is given as a solid line in the Thomson-scattering brightness profile of Figure 7 and as a dotted line in the Thomson-scattering brightness profile of Figures 8, 9, and 10 in Section 4. Discussion of the significance of the comparison of data and model is deferred to Section 4 below.

3.1.2. Model for Coronal Faraday Rotation

In our model for the background coronal plasma, we assume that the plasma density depends only on the heliocentric distance [r] and that the magnetic field is entirely radial, with its magnitude depending solely on r. Frequently, the coronal magnetic field is approximated using some form of the *Dipole plus Current Sheet* (DCS) magnetic field (Gleeson and Axford, 1976) – sometimes called a split monopole because of its topology – or the *Dipole plus Quadrupole plus Current Sheet* (DQCS) model of Banaszkiewicz, Axford, and McKenzie (1998), which adds a weak quadrupole term to the DCS model. At these heliocentric distances, however, a radial magnetic field is a good approximation (see, *e.g.*, Banaszkiewicz, Axford, and McKenzie, 1998). However, we do retain the coronal current sheet of the DCS model as an infinitely thin neutral line, where the polarity of the coronal magnetic field reverses, located at an angle β_c. This geometry is demonstrated in Figure 1.

As discussed in Section 1.1, the angle β_c is crucial; the magnitude of the observed rotation measure is critically dependent on this parameter. To determine β_c, we used the same procedure outlined by Kooi *et al.* (2014): a Python program was used to project the LOS for a given source onto heliographic coordinates. Maps of the coronal magnetic field (determined by a potential-field source-surface model with the surface at $r = 3.25\ \mathrm{R}_\odot$) were obtained from the online archive of the Wilcox Solar Observatory (WSO). The digital form of these maps was used to determine the heliographic coordinates of the coronal neutral line. The value of β at which these two curves intersected gave the parameter β_c. For further details, see Mancuso and Spangler (2000) and Ingleby, Spangler, and Whiting (2007).

Because our observations were made during solar-maximum conditions, the neutral line has a complex geometry and crosses the LOS for several sources from our August 2012 observations multiple times; however, for 0842, 0843, and 0846, the associated LOS only cross one neutral line, as shown in Figure 1. Under these symmetric conditions, the contributions to the integral in Equation (1) from zones B and C cancel each other out, while those of A and D make equal contributions of the same sign. The LOS to 0900, however, crosses two neutral lines, and this second crossing must be accounted for to properly model the background coronal Faraday rotation to this source.

We use the same form for the coronal plasma density as Equation (6), with $\alpha = 2.36$ and N_0 determined from the least-squares fit to the background coronal $\mathrm{B_T}$ as described in Section 3.1.1. For the coronal magnetic field, we use the single power-law representation that appears in Kooi *et al.* (2014):

$$\boldsymbol{B}(r) = B_0 r^{-\delta} \hat{\boldsymbol{e}}_{\boldsymbol{r}}, \tag{8}$$

where r is in units of $\mathrm{R}_\odot$ and B_0 and δ are taken from the model of Sakurai and Spangler (1994a): $B_0 = 1.01$ G and $\delta = 2$. The constant B_0 can be of either polarity and reverses sign at the coronal current sheet. From Equation (1), the resulting expression for rotation measure [RM] is

$$\mathrm{RM} = \left[\frac{2C_{FR}\mathrm{R}_\odot N_0 B_0}{(\gamma - 1)R_0^{\gamma-1}}\right]\left(\cos^{\gamma-1}\beta_{c,1} - \cos^{\gamma-1}\beta_{c,2}\right), \tag{9}$$

where $C_{FR} \equiv e^3/2\pi m_\mathrm{e}^2 c^4$, $\gamma \equiv \alpha + \delta$, and R_0 is defined in Figure 1 and given in solar radii. $\beta_{c,1}$ and $\beta_{c,2}$ give the locations of the first and second neutral lines; consequently, for LOS to sources such as 0900, the second crossing at $\beta_{c,2}$ serves to reduce the magnitude of the observed RM. The sign of the rotation measure depends on the polarity of $\boldsymbol{B}$ for $\beta < \beta_{c,1}$ and the relation between $\beta_{c,1}$ and $\beta_{c,2}$:

i) If $|\beta_{c,1}| > |\beta_{c,2}|$: then RM > 0 when $B_0 > 0$ for $\beta < \beta_{c,1}$, otherwise RM < 0.
ii) If $|\beta_{c,1}| < |\beta_{c,2}|$: then RM < 0 when $B_0 > 0$ for $\beta < \beta_{c,1}$, otherwise RM > 0.

For LOS that only cross one neutral line, $\beta_{c,2} \equiv \pi/2$ and Equation (9) reduces to Equation (9) of Kooi *et al.* (2014). The expression Equation (9) is in cgs units. For MKS units (the conventional units of $\mathrm{rad\,m^{-2}}$), the number resulting from Equation (9) should be multiplied by 10^4.

We do not perform a least-squares fit to determine the magnitude of B_0, but we elect to use the same value, $B_0 = 1.01$ G, as above because we only have at most two to three radioastronomical scans of 0842, 0843, and 0900 before they were occulted by CMEs; the only parameter calculated from a fit to data in Equation (9) is N_0. Consequently, the RM curve for the background corona is a *prediction* and not a fit. The RM curve for the background coronal plasma given by Equation (9) is shown as a solid line in the RM(t) profile of Figure 7 and as a dotted line in the RM(t) profile of Figures 8, 9, and 10. Table 3 gives the range in values for β_c and the N_0 determined for each source, the extrapolated plasma density at 1 AU, n_e ($r = 1$ AU), and for completeness B_0. The N_0 determined for 0842 and 0846 are consistent with each other; however, N_0 for 0843 is somewhat smaller, most likely because the LOS to this source sampled the dimmest region of the corona relative to the other sources, before occultation by CME-1. Similarly, N_0 for 0900 is somewhat larger because the source LOS samples the edge of a bright streamer before occultation (*e.g.* see Figure 4). To compare the N_0 values to the plasma density measured *in situ* at 1 AU, we assume Equation (6) holds out to 10 $\mathrm{R}_\odot$, then extrapolate out to 1 AU with $n_\mathrm{e}(r) \propto r^{-2}$; the extrapolated plasma densities in Table 3 range from 2.1 cm^{-3} to 4.0 cm^{-3}. Over the period of 2 August through 6 August 2012, the *Charge, Element, and Isotope Analysis System* (CELIAS) *Proton Monitor* (PM) onboard SOHO measured a range of proton densities (1.3 – 13.5 cm^{-3}) with a mean value of $\approx$4.6 cm^{-3}. While our values for N_0 in Table 3 are lower than the original model value of $N_0 = 1.83 \times 10^6\ \mathrm{cm}^{-3}$ used by Sakurai and Spangler (1994a), our values are consistent with CELIAS-PM plasma-density data for this period; however, this calculation is contingent on the heliocentric distance at which $n_\mathrm{e}(r) \propto r^{-2}$. Further discussion and comparison between data and model is deferred to Section 4 below.

3.2. Faraday Rotation through a Force-Free Flux Rope

We model the CME as a cylindrically symmetric force-free flux rope with a magnetic field composed of an axial and azimuthal field (*e.g.* see Gurnett and Bhattacharjee, 2006):

$$\boldsymbol{B} = B_\mathrm{CME}\big[J_0(\alpha\rho)\hat{\boldsymbol{e}}_\mathbf{z} + H J_1(\alpha\rho)\hat{\boldsymbol{e}}_{\boldsymbol{\phi}}\big], \tag{10}$$

where B_CME is the magnitude of the magnetic field along the central flux-rope axis, H specifies the helicity ($H = -1$ for left-handed and $H = +1$ for right-handed helicities), J_0 and J_1 are the zeroth- and first-order Bessel functions of the first kind, respectively, and the coordinates are given in axis-centered cylindrical coordinates $(\hat{\boldsymbol{e}}_{\boldsymbol{\rho}}, \hat{\boldsymbol{e}}_{\boldsymbol{\phi}}, \hat{\boldsymbol{e}}_\mathbf{z})$. For a flux rope with radius R_CME, we define $\alpha R_\mathrm{CME} \equiv 2.405$, the first zero of J_0, to ensure that the axial field is zero at the surface of the flux rope. By employing Equation (10), we are assuming that the CME can be approximated by a cylinder on the scales of the LOS penetration of the CME, and we do not account for the CME curvature on global scales.

Equation (10) is given in the axis-centered reference frame of the CME. Two Euler rotations are necessary to convert the axis-centered reference frame into the Sun–LOS reference frame. Figure 6 shows an illustration of the Sun–LOS reference frame: in Cartesian coordinates, the unit vectors $\hat{\boldsymbol{e}}_\mathbf{x}$ and $\hat{\boldsymbol{e}}_\mathbf{y}$ lie in the plane defined by the LOS and the Sun (Figure 6b), and $\hat{\boldsymbol{e}}_\mathbf{z}$ is perpendicular to this plane (Figure 6a), with the origin [O] centered at the point where the central axis of the CME intersects this plane. Figure 6 also defines the three angles that are important in determining the LOS magnetic-field component: θ_z is the angle that the axial-magnetic field [B_z] makes with respect to the Sun–LOS plane and is defined as positive for a rotation toward the LOS; ϕ_z is the angle by which the semi-major axis of the tilted flux rope has been rotated in the Sun–LOS plane; and β_CME is the angle at which the flux rope was ejected from the Sun. A flux rope with $\theta_\mathrm{z} = 0°$ is oriented perpendicular to the Sun–LOS plane, and the axial-field contribution to Faraday rotation will be zero. Similarly, a flux rope with $\theta_\mathrm{z} = 90°$ and $\phi_\mathrm{z} = 0°$ has an axial field aligned with the LOS, and the azimuthal contribution will be zero.

Figure 6 also shows the limits $x_\pm$ and $y_\pm$. The points closest to and farthest from the observer at which the LOS intercepts the boundary of the flux rope are x_+ and x_-, respectively. The points at which the LOS first enters and finally exits the flux rope are y_+ and y_-, respectively. Finally, R_0 is the impact parameter, R_CME is the radius of the flux rope, and y_p gives the penetration length and is the distance from the leading edge of the CME to the LOS; R_CME and y_p are measured using the LASCO-C3 images, as discussed in Section 2.6.

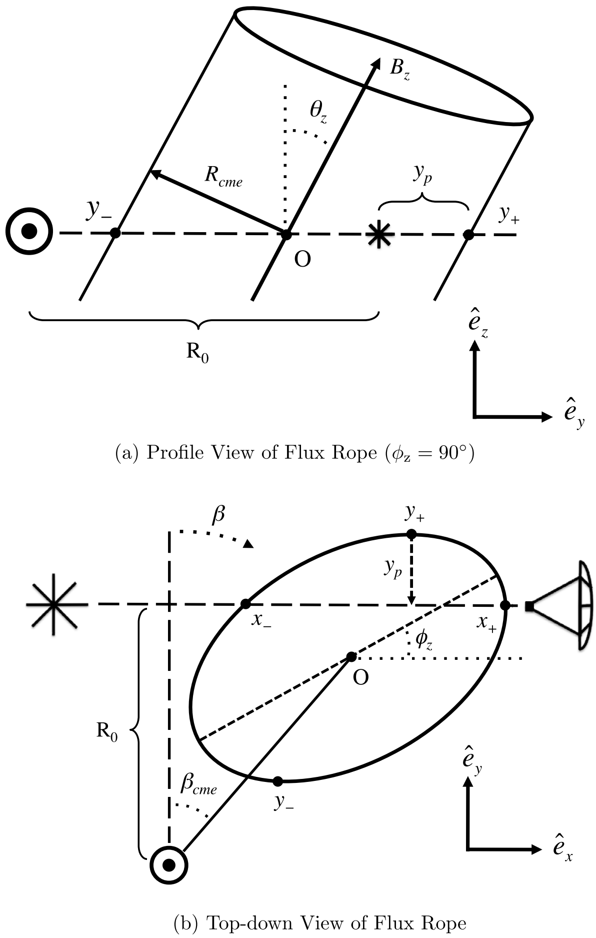

(a) Profile View of Flux Rope ($\phi_z = 90°$)

(b) Top-down View of Flux Rope

Figure 6 Illustration of the LOS from a radio source, through a flux rope CME, to a radio telescope on Earth. The LOS passes at a closest distance, or impact parameter, R_0. The axial field [B_z] of the flux rope is rotated by θ_z with respect to the plane defined by the LOS and the Sun, and the ellipse is the projection of the (tilted) flux rope on this plane; the small dashed line gives the semi-major axis of the projection. O is the point of intersection between the plane and the central axis of the flux rope. ϕ_z gives the rotation of the semi-major axis with respect to the LOS. $x_\pm$ are the points at which the LOS intercepts the boundary of the flux rope, and $y_\pm$ give the maximum extent of the flux rope as measured from the central axis in the Sun–LOS coordinate system. y_p gives the penetration length and is the distance from the leading edge of the CME to the LOS. The figure illustrates an idealization that is employed in this article, which is that the CME emerges from and continues to follow the coronal neutral line [$\beta_{CME} = \beta_c$], the solid line from the Sun to O.

Substituting Equation (10) into Equation (1) and making the necessary rotations gives

$$\mathrm{RM}_{\mathrm{CME}} = C_{\mathrm{CME}} \int_{\tilde{u}_-}^{\tilde{u}_+} \left[J_0(\alpha R_{\mathrm{CME}} \tilde{\rho}) \cos\phi_z \tan\theta_z - H J_1(\alpha R_{\mathrm{CME}} \tilde{\rho}) \frac{\tilde{y}}{\tilde{\rho}} \right] \mathrm{d}\tilde{u} \tag{11}$$

and

$$\tilde{u}_\pm = \frac{-\tilde{y} \sin\phi_z \cos\phi_z \sin\theta_z \tan\theta_z \pm \sqrt{1 - \tilde{y}^2 + \sin^2\phi_z \tan^2\theta_z}}{1 + \sin^2\phi_z \tan^2\theta_z} \tag{12}$$

$$\tilde{\rho}^2 = a_1(\phi_z, \theta_z)\tilde{u}^2 + a_2(\phi_z, \theta_z)\tilde{u}\tilde{y} + a_3(\phi_z, \theta_z)\tilde{y}^2, \tag{13}$$

where $a_1(\phi_z, \theta_z) = 1 + \sin^2\phi_z \tan^2\theta_z$, $a_2(\phi_z, \theta_z) = \sin 2\phi_z \sin\theta_z \tan\theta_z$, and $a_3(\phi_z, \theta_z) = \cos^2\theta_z + \cos^2\phi_z \sin^2\theta_z$ and $\phi_z \in [0, 2\pi], \theta_z \in [-\pi/2, \pi/2]$. In Equation (11), the coefficient is $C_{\mathrm{CME}} = C_{\mathrm{FR}} N_{\mathrm{CME}} B_{\mathrm{CME}} R_{\mathrm{CME}}$ and the integration variable is $\tilde{u} \equiv \tilde{x} \cos\theta_z$. The variables $\tilde{x}$, $\tilde{y}$, and $\tilde{\rho}$ are dimensionless and have been scaled by R_{CME}. In this calculation, we have assumed that the plasma density [N_{CME}] is constant through the flux-rope structure to simplify analysis. In relation to Figure 6, $\tilde{u}_\pm = x_\pm \cos\theta_z / R_{\mathrm{CME}}$ and $\tilde{y} = \sqrt{1 + \sin^2\phi_z \tan^2\theta_z} - y_p / R_{\mathrm{CME}}$. The maximum and minimum values that $\tilde{y}$ attains are

$y_\pm/R_{\mathrm{CME}} = \pm\sqrt{1+\sin^2\phi_z \tan^2\theta_z}$, which comes from the requirement that at the instant the LOS is tangent to the surface of the flux tube: $x_+ = x_-$. In measuring R_{CME}, we emphasize that y_+ is associated with the *leading edge of the outer loop*, and y_- is associated with the boundary between the inner cavity and the bright core, whereas models that describe the outer loop as a plasma-sheath region may associate y_+ with the boundary between the outer loop and the inner cavity. Equation (11) reproduces Figure 3 of Liu *et al.* (2007) for $\phi_z = 0$ and letting y_{p} be determined by the CME velocity and β_{CME}.

Because we have assumed that the plasma density is constant inside the flux tube, the Thomson-scattering brightness is given simply by

$$\mathrm{B_T}/\mathrm{B}_\odot = \left(\frac{3\sigma_T \mathrm{R}_\odot N_{\mathrm{CME}}}{64 R_0}\right)\left[6(\beta_+ - \beta_-) - (\sin 2\beta_+ - \sin 2\beta_-)\right], \tag{14}$$

where $\beta_\pm$ are the angles to $x_\pm$ in the β-coordinate defined in Figures 1 and 6b and are given by

$$\tan\beta_\pm = \left[1 - \left(\frac{R_{\mathrm{CME}}/\mathrm{R}_\odot}{R_0}\right)\tilde{y}\right]\tan\beta_{\mathrm{CME}} + \left(\frac{R_{\mathrm{CME}}/\mathrm{R}_\odot}{R_0}\right)\tilde{x}_\pm. \tag{15}$$

Between Equations (11) and (14), there are six free parameters: β_{CME}, θ_z, ϕ_z, N_{CME}, H, and B_{CME}. We determined these parameters for CME-1 and CME-2 using the following method:

i) We assume $\beta_{\mathrm{CME}} = \beta_{\mathrm{c}}$. As discussed in Section 2.2, both CME-1 and CME-2 were ejected near the coronal neutral line determined from the WSO potential-field source-surface model, and consequently, we assume the CMEs continue to follow the neutral line out to a given source's LOS.
ii) We calculate θ_z from the LASCO-C3 images by measuring the angle that the leading edge makes with the Sun–LOS plane (*e.g.* see Figure 6a). To do this, we assume (1) the leading edge is parallel to the central axis and (2) the measured angle is not subject to significant projection effects. The latter assumption would not be valid if β_{CME} were large; however, β_{CME} must be small, otherwise geometric projection effects would make the three-part structure of CME-1 and CME-2 difficult to decipher (*e.g.* at large β_{CME} values, CME-1 and CME-2 would become partial halo CMEs). These assumptions are required to eliminate the Faraday-rotation degeneracy between the CME's orientation and handedness.
iii) Because we have assumed that the flux rope is ejected at an angle $\beta_{\mathrm{CME}} = \beta_{\mathrm{c}}$ and we further assume the semi-major axis of the flux rope in the Sun–LOS plane is oriented in the same direction, then $\phi_z = \pm 90^\circ - \beta_{\mathrm{c}}$ where $\pm$ refers to CMEs ejected from the western and eastern solar limbs, respectively.
iv) We determined N_{CME} by performing a least-squares fit of Equation (14) to the Thomson-scattering brightness (after removing the model background coronal contribution).
v) We selected the sign for the flux-rope helicity $[H]$ to give the appropriate magnetic polarity for the LOS magnetic-field geometry required by the rotation-measure time series.
vi) We determined B_{CME} by performing a least-squares fit of Equation (11) to the rotation-measure time series using the previously calculated N_{CME} (again, after removing the model background coronal contribution).

In removing the model background coronal contribution, it is important to account for the region along the LOS within the flux rope. The same method was also applied for CME-3; however, because CME-3 does not have a three-part structure, we additionally assume that

$R_{\mathrm{CME}} \approx 3\ \mathrm{R}_{\odot}$, which is within the range of R_{CME} measured for CME-1 and CME-2 (see Table 4).

The values determined for β_{CME}, θ_{z}, ϕ_{z}, N_{CME}, H, and B_{CME} for each CME appear in Table 4, as well as the time range over which data from the Thomson-scattering time series [$\mathrm{B}_{\mathrm{T}}(t)$] and rotation measure time series [$\mathrm{RM}(t)$] were used to determine these fit parameters. The errors reported for θ_{z} give the range over which θ_{z} varied during the observations, and the errors reported for N_{CME} and B_{CME} are the statistical uncertainty in determining these parameters. The $\mathrm{B}_{\mathrm{T}}(t)$ and $\mathrm{RM}(t)$ curves for the flux-rope models corresponding to these values are shown as dashed lines in Figures 8, 9, and 10 in Section 4. Further discussion of the significance of the comparison of data and model is deferred to Section 4 below.

4. Comparison of Observations with Coronal and CME Models

We begin by demonstrating our background coronal model's capability to reproduce observations of 0846 because our ability to estimate the background corona is crucial for correctly applying the CME model and interpreting the CME data. We then employ a single-flux-rope model to reproduce observations of 0842 and 0900. Finally, we use a two-flux-rope model (corresponding to CME-1 and CME-2) to reproduce observations of 0843.

4.1. 0846: Coronal Occultation Only

The time series of Thomson brightness [$\mathrm{B}_{\mathrm{T}}(t)$] and coronal Faraday rotation [$\mathrm{RM}(t)$] of the source 0846 are shown together in Figure 7 along with fits to the data determined from the coronal power-law models for n_{e} and $\boldsymbol{B}$ discussed in Section 3.1. The Thomson brightness diminishes slowly over the course of the observing session as the solar impact parameter for 0846 increases from 11.1 $\mathrm{R}_{\odot}$ at 15:06 UT to 11.4 $\mathrm{R}_{\odot}$ at 21:11 UT. While fluctuations are present, the data do not deviate significantly from the fit and only range in value from $1-2 \times 10^{-12}\ \mathrm{B}_{\odot}$, suggesting that no transient white-light structures occulted the LOS. The lack of apparent white-light structures in these data over the course of the observing session supports our assertion that 0846 was not occulted by a CME or other similarly complex plasma structures on August 2. Therefore, 0846 demonstrates the effects from the background coronal plasma only and serves as a reference for comparison to sources occulted by CMEs.

The data for the rotation measure on a scan-by-scan basis show that the RM remained relatively constant during this observing session. The solid points (Hot Spot 1) give the RM determined for the strongly polarized northern lobe of 0846, and the open symbols (Hot Spot 2) give the RM determined for the weaker southern lobe; the error bars represent the propagation of radiometer noise and are larger for the southern lobe because of its weaker polarized intensity (see Section 2.5). The $\mathrm{RM}(t)$ for the northern and southern lobes are consistent with each other. $\mathrm{RM}(t)$ could not be determined for the other two components, the northern hotspot and southern jet described in Section 2.1, because their polarized intensities were too small; however, a mean RM for the whole observing session on 2 August was calculated for both components: the mean RM for the northern hotspot and southern jet were $-0.44 \pm 0.52\ \mathrm{rad\,m^{-2}}$ and $-0.41 \pm 0.98\ \mathrm{rad\,m^{-2}}$, respectively. These are consistent with the $\mathrm{RM}(t)$ for the northern and southern lobes.

The $\mathrm{RM}(t)$ are small (*e.g.* $-0.95 \pm 0.32\ \mathrm{rad\,m^{-2}}$ and $-0.73 \pm 0.29\ \mathrm{rad\,m^{-2}}$ for the northern and southern lobes, respectively, at 18:06 UT). The model RM (solid curve in Figure 7),

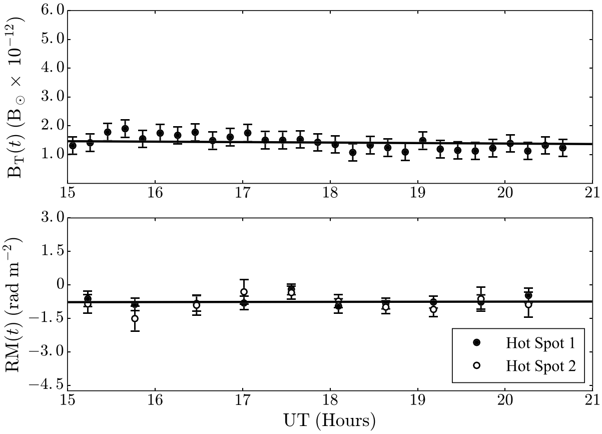

Figure 7 Thomson-scattering brightness (top) and coronal RM(t) (bottom) for 0846 on 2 August 2012. Thomson brightness is given for one LOS to the target source center; RM(t) is given for the LOS for Hot Spot 1 and Hot Spot 2. Each brightness measurement is taken from one LASCO-C3 image. Each RM measurement is determined from all seven bandpasses for a given scan (≈ three minutes duration). The solar impact parameter [R_0] increases from 11.1 $R_\odot$ at 15:06 UT to 11.4 $R_\odot$ at 21:11 UT. The superposed curves are fits determined from the coronal models for n_e and $\boldsymbol{B}$. This source was occulted by the coronal plasma only and serves as a reference for comparison to sources occulted by CMEs.

which was determined from the fit for plasma density from the Thomson-brightness data, and a coronal magnetic-field model given in detail in Section 3.1, agrees well with the measured RM(t) over the entire observing session. These small RM(t) can be qualitatively understood as a consequence of the geometry involved in making these measurements: 0846 is at large heliocentric distances where coronal Faraday rotation is expected to be at most on the order of a few rad m^{-2}.

Figure 7 is particularly important in context here as it demonstrates our ability to model the background coronal plasma. The model B_T and RM profiles (solid lines in Figure 7) agree well with the measured data; this suggests that Equations (7) and (9) are sufficient for modeling the Thomson-scattering brightness and rotation-measure contributions from the background corona.

4.2. 0842 and 0900: Occultation by a Single CME

In this section, we describe the results for the two sources, 0842 and 0900, that were occulted by a single CME. 0842 is a strongly polarized point source and thus provides one LOS through the plasma structure of CME-2. Figure 8 shows the Thomson brightness and coronal Faraday rotation to 0842 together with the model for the background corona alone (dotted curve), the flux-rope model for the CME alone (dashed curve), and the sum of the contributions from both models (solid curve). In these fits, $\phi_z \approx 90° - \beta_{\mathrm{CME}} = 90° - \beta_c$ where β_c ranges in value ($-25.4° \leq \beta_c \leq -22.4°$) over the course of the observing session as the LOS geometry changes and $\theta_z \approx -10° \pm 2°$ for the whole observing session. The least-squares fit to B_T gives $N_{\mathrm{CME}} = 6.9 \pm 0.5 \times 10^3$ cm^{-3} and the corresponding fit to RM(t) gives $B_{\mathrm{CME}} = 10.4 \pm 0.4$ mG. These values are summarized in Table 4.

Before occultation by CME-2, the Thomson brightness for 0842 was 60% higher than the Thomson brightness for 0846; this is because 0842 was observed at smaller impact parameters: 9.4 $R_\odot$ – 10.6 $R_\odot$. The trend is the same, however, as the Thomson brightness slowly

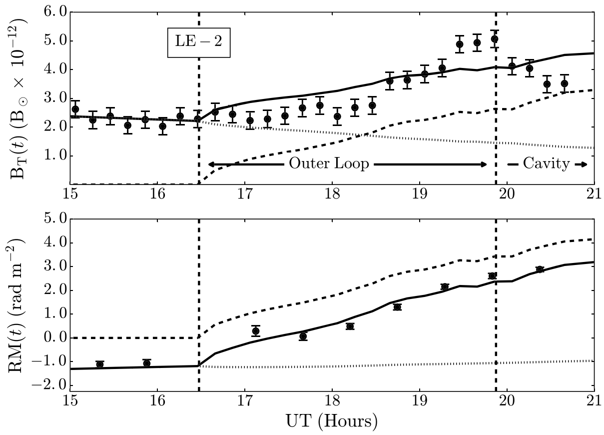

Figure 8 Thomson-scattering brightness (top) and coronal RM(t) (bottom) for 0842 on 2 August 2012. The dotted curve represents the background coronal model, the dashed curve represents the single-flux-rope model, and the solid curve represents the sum of the contributions from both models together. Fitted parameters for the flux-rope model are $N_{\mathrm{CME}} = 6.9 \pm 0.5 \times 10^3$ cm^{-3} and $B_{\mathrm{CME}} = 10.4 \pm 0.4$ mG with helicity $H = -1$. The first vertical line (LE-2) gives the time (16:30 UT) at which 0842 was occulted by CME-2, which had the standard three-part structure. The second vertical line gives the boundary between the outer loop and inner cavity.

Table 4 Model parameters for the coronal mass ejections.

Coronal mass ejection	CME-1	CME-2		CME-3
R_{CME} [$R_\odot$][a]	[2.8, 3.8]	[2.5, 4.0]		3.0[b]
β_{CME}[a]	[19.0°, 21.3°]	[−22.4°, −25.4°]		[30.4°, 30.8°]
ϕ_Z	$90° - \beta_{\mathrm{CME}}$	$90° - \beta_{\mathrm{CME}}$		$-90° - \beta_{\mathrm{CME}}$
θ_Z	$80° \pm 5°$[c]	$80° \pm 5°$[c]	$-10° \pm 2°$[d]	45°[e]
Time range for fit [UT][f]	15:42 – 18:30	16:30 – 20:42		17:18 – 20:42
N_{CME} [10^3 cm^{-3}]	21.4 ± 0.6	6.9 ± 0.5		11.2 ± 0.3
B_{CME} [mG]	11.3 ± 0.4	10.4 ± 0.4		2.4 ± 0.3
H	+1	−1		−1

[a] We allowed these parameters to evolve with time over the range provided as the CMEs propagated outward.

[b] CME-3 does not have a three-part structure; consequently, we assume that $R_{\mathrm{CME}} \approx 3$ $R_\odot$, which is within the range of R_{CME} measured for CME-1 and CME-2.

[c] θ_Z for 0843.

[d] θ_Z for 0842.

[e] $\theta_Z = 45°$ is an approximation; the orientation for CME-3 was not clearly defined.

[f] The time range used in determining the model-fit results for CME-1, CME-2, and CME-3 using data for 0843, 0842, and 0900, respectively.

diminishes until the leading edge (LE-2) crosses the LOS at 16:30 UT. 0842 is first occulted by the outer loop of CME-2, represented by an initially slow increase in $B_T(t)$ until 18:06 UT, at which time $B_T(t)$ begins increasing more rapidly before reaching a maximum value of $\approx 5 \times 10^{-12}$ $B_\odot$. At 20:06 UT, the LOS begins penetrating the inner cavity of CME-2;

although there is a corresponding decrease in Thomson brightness [$\mathrm{B_T}(t)$], it remains about a factor of two greater than the background coronal Thomson-scattering model (dotted line in Figure 8).

The $\mathrm{RM}(t)$ for 0842 also demonstrate a strong signal associated with the passage of CME-2. Before occultation, the $\mathrm{RM}(t)$ is near $-1\ \mathrm{rad\,m^{-2}}$ and is in very good agreement with the model RM for the background corona determined in the same way as for 0846 (see Section 3.1). After occultation by the outer loop of CME-2, the $\mathrm{RM}(t)$ changes sign and increases gradually to $2.60 \pm 0.11\ \mathrm{rad\,m^{-2}}$. The sign change implies that the density enhancement associated with the increasing Thomson-brightness profile will not be sufficient to account for the increasing $\mathrm{RM}(t)$; the magnetic-field structure must also be fundamentally different to produce a sign change in the magnetic-field component parallel to the LOS. Once the LOS begins to sample the inner cavity, $\mathrm{B_T}(t)$ decreases, corresponding to a decrease in the plasma density; however, the $\mathrm{RM}(t)$ increases to $2.88 \pm 0.09\ \mathrm{rad\,m^{-2}}$, for a total change of $+4.0\ \mathrm{rad\,m^{-2}}$ over the background coronal RM. This implies an enhancement in the magnetic fields sampled by the LOS. We did observe 0842 at 16:35 UT, shortly after occultation by the leading edge in white-light LASCO-C3 data. The measured RM, -21.95 ± 3.11, dwarfed the values presented in Figure 8; however, the Stokes I, Q, and U maps for this scan are very poor in quality, having $\gtrsim 20\times$ the noise of the other scan maps.

The background models in Figure 8 are given by Equations (7) and (9) before occultation by LE-2; however, the background models in Figure 8 remove the contribution by the coronal n_{e} and $\boldsymbol{B}$ along the section of the LOS within the flux rope (*i.e.* the coronal-plasma model along this section of the LOS is replaced by the flux-rope model). The single-flux-rope model reproduces the general increase in Thomson-scattering brightness, but does not reproduce the $\approx 1 \times 10^{-12}\ \mathrm{B_\odot}$ fluctuations present after CME-2 occults the LOS. These fluctuations are much larger than the fluctuations in the background coronal $\mathrm{B_T}(t)$ profile and are likely real. The model overestimates $\mathrm{B_T}(t)$ near the beginning of the occultation and after the LOS begins to sample the inner cavity; the model also underestimates $\mathrm{B_T}(t)$ during the peak occultation by the outer loop. It is not surprising that the model produces a "mean" profile and does not reproduce the fast ramp and decay in $\mathrm{B_T}(t)$ because we have assumed that the plasma density is constant over the flux rope.

The single-flux-rope model reproduces the $\mathrm{RM}(t)$ data, both in sign and magnitude, for 0842. The background model suffices for determining the RM values before occultation; after occultation, the addition of the flux-rope model (with helicity $H = -1$) is necessary to reproduce the sign change from negative to positive near 17:08 UT. For the θ_{z}, ϕ_{z}, β_{CME}, and H determined for this flux rope, the LOS geometry is such that the azimuthal component of the magnetic field dominates the flux-rope contribution, providing the positive RM necessary to match the $\mathrm{RM}(t)$.

The model appears to fit the $\mathrm{RM}(t)$ profile better, and deviations from this fit appear to be less significant than the deviations in the $\mathrm{B_T}(t)$ profile. The error in $\mathrm{B_T}(t)$ is comparable to the RMS deviations from the background coronal model for $\mathrm{B_T}(t)$ and is on the order of $0.3 \times 10^{-12}\ \mathrm{B_\odot}$. Consequently, the deviations in the $\mathrm{B_T}(t)$ profile after occultation by CME-2 are $2-3$ times the error. This is at most comparable to the deviations in the $\mathrm{RM}(t)$ profile, which should be true because the RM measurements have a smaller footprint (restoring beam) in the corona and are more sensitive to true fluctuations associated with the internal structure of the CME.

While 0842 was occulted by a CME with the standard three-part structure, 0900 was occulted by the narrow, jet-like CME-3 (despite lacking the standard three-part structure, CME-3 is still a mass ejection from the corona). Unlike 0842, 0900 is an extended radio source (see Figure 2) and provides multiple LOS through CME-3. We report the RM data for

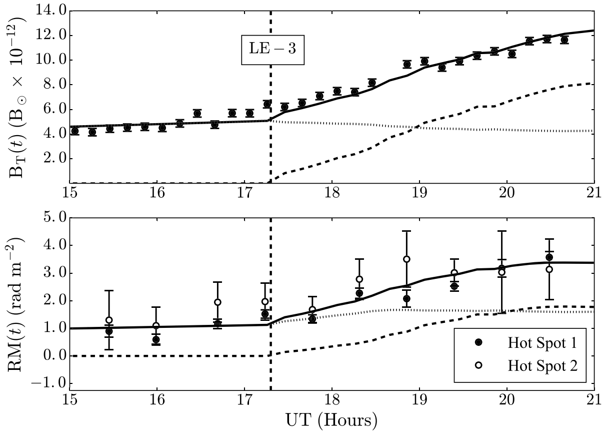

Figure 9 Thomson-scattering brightness (top) and coronal RM(t) (bottom) for 0900 on 2 August 2012. The Thomson brightness is given for one LOS to the target source center; RM(t) is given for the LOS for Hot Spot 1 and Hot Spot 2. The dotted curve represents the background coronal model, the dashed curve represents the single-flux-rope model, and the solid curve represents the sum of the contributions from both models together. The fitted parameters for the flux-rope model are $N_{\mathrm{CME}} = 11.2 \pm 0.3 \times 10^3\ \mathrm{cm}^{-3}$ and $B_{\mathrm{CME}} = 2.4 \pm 0.3$ mG with helicity $H = -1$. The first vertical line (LE-3) gives the time (17:18 UT) at which 0900 was occulted by CME-3, which had the jet-like structure of a narrow CME.

the hot spot in the northern and southern lobes with the strongest polarization in Figure 9, along with the Thomson-brightness profile, together with the model for the background corona alone (dotted curve), the flux-rope model for the CME alone (dashed curve), and the sum of the contributions from both models (solid curve). This source was occulted by two neutral lines, one on the Earth-side and one on the far side of the Sun. We chose $\phi_z \approx -90^\circ - \beta_{\mathrm{CME}} = -90^\circ - \beta_c$ corresponding to the neutral line on the Earth-side of the Sun ($30.4^\circ \leq \beta_c \leq 30.8^\circ$) because CME-3's initiation point was on the Earth-side of the Sun. We approximated $\theta_z \approx 45^\circ$ for the whole observing session; however, θ_z for CME-3 was not as clearly defined as it was for CME-2. The least-squares fits to $B_T(t)$ and RM(t) give $N_{\mathrm{CME}} = 11.2 \pm 0.3 \times 10^3\ \mathrm{cm}^{-3}$ and $B_{\mathrm{CME}} = 2.4 \pm 0.3$ mG. These parameters are summarized in Table 4. While we report a positive B_{CME} and negative helicity for CME-3 in Table 4, the geometry of CME-3 is difficult to define (particularly θ_z), and consequently, B_{CME} and helicity may be negative and positive, respectively.

Of the sources discussed in this article, 0900 had the smallest impact parameters, ranging from 8.6 $R_\odot$ near the beginning of the observing period to 8.0 $R_\odot$ near the end. It is therefore no surprise that the Thomson brightness associated with the background corona is largest for this source. Furthermore, the general trend of the background $B_T(t)$ and RM(t) to increase slowly over time is a result of the slow decrease in the impact parameter. After the leading edge, LE-3, of CME-3 occults 0900, the Thomson brightness increases at a faster rate, approaching $\approx 12 \times 10^{-12}\ B_\odot$, which is twice the predicted coronal value of $\approx 6 \times 10^{-12}\ B_\odot$ (dotted line in Figure 9).

The RM transient signal in the RM(t) for 0900 is not as strong as the signal present in the RM(t) for 0842. The RM is $\approx +1\ \mathrm{rad\,m^{-2}}$ at the beginning of the observing period and is in good agreement with the model for the background corona. 0900 is the only source presented in this article that has RM > 0 for the background corona; this is because the LOS samples a different region of the corona on the opposite side of the Sun (see Figure 2). In particular, the LOS to 0900 crosses two magnetic neutral lines, not just one, as is the case for the other three sources (see Section 3.1.2).

The difference between the RM(t) before and after occultation by CME-3 is subtle and manifests as a small increase in the rate of increasing RM; there is no sign change (as is the case in Figure 8) and the total change in RM over the whole session is $\approx 2.7\ \mathrm{rad\,m^{-2}}$. This increase, although small, is detected by the strongest hot spot in the southern lobe: Hot Spot 1 in Figure 9. This southern hot spot has the strongest polarized intensity ($P = 18.48 \pm 0.14\ \mathrm{mJy\,beam^{-1}}$) for this source and therefore it has small error bars. The detection is not obvious in the RM(t) of the northern hot spot because of its small polarized intensity ($P = 7.12 \pm 0.14\ \mathrm{mJy\,beam^{-1}}$) and correspondingly large error bars; however, the RM(t) of the northern hot spot is consistent with the southern hot spot. Without the additional, independent data provided by the LASCO-C3, COR2-A, and COR2-B instruments, it would be difficult to interpret this RM(t) as a coronal transient.

As with Figure 8, the background coronal models remove the contribution by the coronal n_e and $\boldsymbol{B}$ along the section of the LOS within the flux rope. Consequently, before occultation by LE-3, the background model takes the same value as Equations (7) and (9), and after occultation by LE-3, the background coronal model values deviate. The background model $\mathrm{B_T}$ decreases because we have effectively removed a small fraction of the sum over plasma density. The background model RM *increases* as a consequence of the geometry of the LOS: the LOS magnetic field is negative over the majority of the LOS removed to account for the presence of the flux rope, and therefore a negative RM is removed, resulting in a background model RM with a larger positive magnitude.

The single-flux-rope model satisfactorily reproduces the general trends in both the Thomson-scattering brightness and the rotation-measure profiles. Deviations from the model $\mathrm{B_T}(t)$ after occultation by CME-3 are similar to the deviations before occultation and are most likely representative of the uncertainty in measuring $\mathrm{B_T}(t)$ and not of significant deviations from the model. The model very likely provides a better fit in this case than for the $\mathrm{B_T}(t)$ profile of 0842 because of the jet-like appearance of CME-3: the LOS is not obviously occulted by a bright outer loop and then a dark inner cavity (as is the case for 0842); it is only occulted by a bright jet-like outflow of plasma.

Similar to 0842, the model RM agrees well with the RM(t) data, and there are no significant deviations, especially in the RM(t) for the strongly polarized southern lobe; however, B_{CME} is smaller, largely because the differences between the pre- and post-occultation magnitudes in the profiles for 0900 are smaller than they are for 0842. The model RM for 0900 is also insensitive to the parameter θ_z; letting θ_z range in value from 0° to 80° changes N_{CME} and B_{CME} by less than a factor of two. The azimuthal magnetic field dominates regardless of θ_z because the measured penetration length [y_p] for CME-3 is small.

The agreement between the model and the measured RM(t) for 0900 is important for two reasons. First, like 0846, this demonstrates our ability to accurately model the effects of the background coronal plasma; however, 0846 was only occulted by one neutral-line and 0900 is occulted by two neutral lines. If we had not accounted for the second neutral line crossing in Equation (9), the model value for the background coronal RM would more than double because of the LOS geometry, producing a large discrepancy between model and measurement. The second important feature is that our background coronal model correctly predicts RM > 0 for 0900 and RM < 0 for the other sources, suggesting that our background coronal models do not have a systematic bias toward negative rotation measures.

4.3. 0843: Occultation by Two CMEs

In this section, we describe the results for 0843, which was occulted by the outer loops of two CMEs on 2 August 2012. Kooi (2016) demonstrated that a single-flux-rope model is not sufficient to reproduce the observed Thomson-brightness and coronal Faraday-rotation data because such a model overestimates both the Thomson-scattering brightness and the rotation-measure time series beginning after 19:00 UT. The observed $\mathrm{RM}(t)$, in particular, diverges significantly from a single-flux-rope model. The inability of a single-flux-rope model to reproduce the results of our observations suggests that we must account for both of the CMEs that occulted 0843.

To model the effect of two flux ropes occulting the LOS to 0843, we need to determine N_{CME} and B_{CME} for both CMEs that occulted the LOS: CME-1 and CME-2. For CME-1, in performing the least-squares fit to $\mathrm{B_T}(t)$ and $\mathrm{RM}(t)$, we only fit to the data between 15:42 UT and 18:30 UT while the LOS was only occulted by CME-1 alone; the solutions give $N_{\mathrm{CME}} = 21.4 \pm 0.6 \times 10^3\ \mathrm{cm}^{-3}$ and $B_{\mathrm{CME}} = 11.3 \pm 0.4$ mG with helicity $H = +1$. These values are summarized in Table 4. Fortunately, CME-2 also occulted 0842; consequently, we use the plasma density and axial magnetic-field strength determined from the independent observations of 0842 to model CME-2: $N_{\mathrm{CME}} = 6.9 \pm 0.5 \times 10^3\ \mathrm{cm}^{-3}$ and $B_{\mathrm{CME}} = 10.4 \pm 0.4$ mG with helicity $H = -1$.

In fitting the data for CME-1, $\phi_z \approx 90^\circ - \beta_{\mathrm{CME}} = 90^\circ - \beta_c$ where β_c ranges in value ($19.0^\circ \le \beta_c \le 21.3^\circ$) over the course of the observing session as the LOS geometry changes. The parameter θ_z did not vary much in the cases of 0842 and 0900 because the LOS for those two sources penetrated CME-2 and CME-3 and progressed deeper into these CMEs; however, the LOS to 0843 penetrates the outer loop of CME-1, traces a chord through the outer loop, and exits the backside (*e.g.* Figure 4). Similarly, the LOS samples the outer loop of CME-2, but it does not appear to pierce the inner cavity region. As a consequence, the orientation of the leading edge to the Sun–LOS plane evolves over the course of the observations: $\theta_z \approx 75^\circ$ when the LOS initially penetrates the outer loop of CME-1 (15:42 UT); θ_z increases, approaching 90° when the LOS is halfway through the outer loop of CME-1 (18:00 UT); θ_z decreases, approaching 75° as the LOS exits CME-1 (20:06 UT). For simplicity, the model results we present here use a constant value $\theta_z \approx 80^\circ$ for CME-1. We selected this value because $\theta_z \approx 80^\circ \pm 5^\circ$ for the majority of the observations. While we did investigate the effects of letting θ_z vary over this range in modeling $\mathrm{B_T}$ and $\mathrm{RM}(t)$ (*i.e.* letting θ_z increase from 75° to 90° and then decrease back to 75° over the period of observations, as previously described), there was not a significant difference in the fit values for N_{CME}, B_{CME}, and H.

Although the LOS to 0843 only crosses one neutral line, which we have associated with β_{CME} for CME-1, we assume that CME-2 crosses the LOS at approximately the same angle as 0842: $\beta_{\mathrm{CME}} \approx -24^\circ$ for CME-2. We also assume $\phi_z = 90^\circ - \beta_{\mathrm{CME}}$, applying the appropriate β_{CME} for CME-1 and CME-2. The only flux-rope model parameter that we change for CME-2 is setting $\theta_z \approx 80^\circ$ to approximate the observations of the leading edge LE-2. Similar to CME-1, the true value of θ_z for CME-2 with respect to the LOS to 0843 varied over the course of observations by $\approx \pm 5^\circ$.

Figure 10 shows the results of the two-flux-rope model along with the Thomson-brightness and coronal Faraday-rotation data for 0843. The models are as follows: the background corona alone (dotted curve), the flux-rope model for CME-1 alone (dashed curve), the flux-rope model for CME-2 alone (dash–dotted curve), and the sum of the contributions from all models (solid curve). It is important to emphasize that the model sum (solid line in Figure 10) represents a fit to the observed data up to 18:30 UT. After 18:30 UT, the model

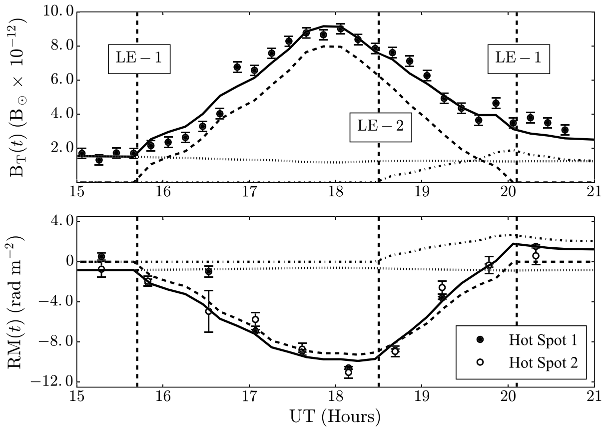

Figure 10 Thomson-scattering brightness (top) and coronal RM(t) (bottom) for 0843 on 2 August 2012. The Thomson brightness is given for one LOS to the target source center; RM(t) is given for the LOS for Hot Spot 1 and Hot Spot 2. The dotted curve represents the background coronal model, the dashed curve represents the flux-rope model for CME-1, the dash–dotted curve represents the flux-rope model for CME-2, and the solid curve represents the sum of the contributions from all models together. The fitted parameters for the flux-rope model associated with CME-1 are $N_{\mathrm{CME}} = 21.4 \pm 0.6 \times 10^3\ \mathrm{cm}^{-3}$ and $B_{\mathrm{CME}} = 11.3 \pm 0.4$ mG with helicity $H = +1$. The fitted parameters for the second flux-rope model are taken directly from the fit to data for 0842. The first and third vertical lines (LE-1) give the times (15:42 UT and 20:06 UT, respectively) at which occultation by CME-1 begins and ends, respectively. The second vertical line (LE-2) gives the time (18:30 UT) at which occultation by CME-2 begins. Both CMEs had the standard three-part structure.

represents a *prediction* based on the model data for CME-1 determined from the fit before 18:30 UT and the model data for CME-2 determined from the independent measurements of 0842 and the background coronal model.

Both the white-light and Faraday-rotation observations for 0843 demonstrate significant transients. The impact parameters for this source, ranging from 9.8 $R_\odot$ at 15:06 UT to 10.5 $R_\odot$ at 21:11 UT, are larger than those of 0900 and comparable to those of 0842; however, the transient signals measured for those two sources are much smaller by comparison. The nominal Thomson-scattering brightness from the background corona is $\approx 1.5 \times 10^{-12}\ B_\odot$ at the beginning of the observing period; after occultation by the leading edge, LE-1, of CME-1 at 15:42 UT, the brightness begins to increase rapidly until it peaks two hours later at $\approx 9.0 \times 10^{-12}\ B_\odot$, six times the value associated with the background corona. $B_T(t)$ begins decreasing after 18:06 UT and continues to do so after occultation by the leading edge, LE-2, of CME-2; this is the same CME that occults the LOS to 0842. Near 20:06 UT, close to the end of the observing period, CME-1 ceases to occult the LOS; however, because CME-2 continues to occult 0843, $B_T(t)$ does not return to the nominal background value, but asymptotes near $3.5 \times 10^{-12}\ B_\odot$, about twice the background model.

The RM(t) profile for 0843 has a V-shaped trend, beginning near $-1\ \mathrm{rad\,m^{-2}}$, peaking near $-11\ \mathrm{rad\,m^{-2}}$ (quite large for these heliocentric distances), and approaching $+1.5\ \mathrm{rad\,m^{-2}}$ at the end of observations. The peak RM during this period ($-10.58 \pm 0.13\ \mathrm{rad\,m^{-2}}$ and $-11.03 \pm 0.57\ \mathrm{rad\,m^{-2}}$ for the southern and northern hot spots, respectively) is more than ten times the coronal contribution predicted as in Section 3.1.2 and is correlated in time with the peak in $B_T(t)$. The $B_T(t)$ "only" increased to six times the coronal contribution, suggesting that the enhancement in plasma density necessary to increase $B_T(t)$ is not sufficient to account for the considerable increase detected in RM(t), and an enhancement in the magnetic-field components along the LOS is required. After peaking at

18:06 UT, the RM(t) for both hot spots decrease, approaching the background coronal value at 19:45 UT near the end of occultation by CME-1. An interesting feature is that the rate of this decrease in magnitude ($\mathrm{dRM}/\mathrm{d}t \approx 6.6\ \mathrm{rad\,m^{-2}\,hr^{-1}}$) is greater than the rate of increase ($\mathrm{dRM}/\mathrm{d}t \approx -3.6\ \mathrm{rad\,m^{-2}\,hr^{-1}}$) earlier in the session. The last scan of 0843 suggests that RM(t) > 0 by the end of the observing session: the measured RM for the strong southern and weaker northern hot spots were $+1.53 \pm 0.14\ \mathrm{rad\,m^{-2}}$ and $+0.36 \pm 0.84\ \mathrm{rad\,m^{-2}}$.

The two-flux-rope model is able to reproduce the observational results of both $\mathrm{B_T}(t)$ and RM(t). Single flux-rope models overestimate $\mathrm{B_T}(t)$ near the end of the observations, during the slow decrease in $\mathrm{B_T}(t)$ after 18:30 UT, because the contribution to the penetration length that is associated with the lower density CME-2 in the two-flux-rope model is associated with the higher density CME-1 in single-flux-rope models. The slow decrease in $\mathrm{B_T}(t)$ is well modeled as the contributions from the diminishing and increasing brightness profiles associated with the passage of CME-1 and CME-2, respectively, in the two-flux-rope model.

The real strength in the two-flux-rope model lies in its ability to represent the RM(t) for 0843. The flux-rope model for CME-1 is consistent with the data before occultation by CME-2; it gives the sign and magnitude for the RM(t), with the exception that it underestimates the peak RM by $\lesssim -1\ \mathrm{rad\,m^{-2}}$. After the second occultation, the two-flux-rope model continues to successfully reproduce the data. Again, we emphasize here that the model data after 18:30 UT is the *prediction* determined from the two-flux-rope model; it is not a fit to the observed data. Two striking features of this model are that i) it fits the fast slope, $\mathrm{dRM}/\mathrm{d}t \approx 6.6\ \mathrm{rad\,m^{-2}\,hr^{-1}}$, and ii) it predicts RM > 0 at the end of the observations. These two features result from the opposing helicities of CME-1 and CME-2. CME-1 has a helicity $H = +1$, as determined from observations of 0843 before 18:30 UT, and CME-2 has a helicity $H = -1$, as determined from the independent observations of 0842. The azimuthal magnetic-field contributions to the RM(t) from CME-1 and CME-2 (the dashed and dash–dotted lines in Figure 10, respectively) are negative and positive, respectively. From 18:30 UT to 20:06 UT, the net effect gives the fast slope in RM(t), and after CME-1 no longer occults 0843 near 20:06 UT, positive RM at the end of the observing session.

These RM data show a key feature that demonstrates an advantage of observing with extragalactic radio sources over pulsars or spacecraft transmitters: 0843 provides two closely spaced LOS with strong linear polarization through CME-1 and CME-2. The LOS to the stronger southern hot spot and the northern hot spot (Hot Spot 1 and Hot Spot 2 in Figure 10) are very close (7.8″, or 5700 km in the corona, which is about twice the FWHM diameter of the synthesized beam), and therefore they sample approximately similar regions of plasma. The strong agreement between the RM(t) for both LOS gives confidence that this large coronal transient is real. Another key feature of these data is their demonstration of the insight gained by employing white-light measurements from multiple vantage points. LASCO-C3 white-light images give a clear view of the propagation of CME-1 (and the corresponding leading edge, LE-1); however, CME-2 is hard to discern in these images because it appears in the background, behind CME-1. The leading edge and structure of CME-2 is clear in COR2-A white-light images, however. It is only with both sets of images that we are able to track the leading edges of CME-1 and CME-2 as their outer loops occult 0843, allowing us to employ a two-flux-rope model.

5. Discussion

The N_{CME} and B_{CME} values determined for the flux-rope models of CME-1, CME-2, and CME-3 represent an enhancement over the measured background values for the corona. The single power-law functions for n_e and $\boldsymbol{B}$ given in Equations (6) and (8) can be evaluated at the location where the neutral line crosses the LOS to provide an estimate of the local plasma density and magnetic-field strength expected for the region occulted by a CME. Using $R_0 \approx 10.2\ \mathrm{R}_\odot$ and $\beta_c \approx 20°$ in the case of 0843 gives $n_e \approx 0.8 \times 10^3\ \mathrm{cm}^{-3}$ and $|\boldsymbol{B}| \approx 8.6$ mG; from Table 4, $N_{\mathrm{CME}} \approx 21.4 \times 10^3\ \mathrm{cm}^{-3}$ and $B_{\mathrm{CME}} \approx 11.3$ mG for CME-1, suggesting an increase in the local plasma density and magnetic-field strength by factors of ≈ 27 and ≈ 1.3, respectively. Similarly, $R_0 \approx 10.0\ \mathrm{R}_\odot$ and $\beta_c \approx -24°$ in the case of 0842 gives $n_e \approx 1.1 \times 10^3\ \mathrm{cm}^{-3}$ and $|\boldsymbol{B}| \approx 8.4$ mG; from Table 4, $N_{\mathrm{CME}} \approx 6.9 \times 10^3\ \mathrm{cm}^{-3}$ and $B_{\mathrm{CME}} \approx 10.4$ mG for CME-2, suggesting an increase in the local plasma density and magnetic-field strength by factors of ≈ 6.3 and ≈ 1.2, respectively.

Observations of 0900, however, only suggest an enhancement in the plasma density. Using $R_0 \approx 8.3\ \mathrm{R}_\odot$ and $\beta_c \approx 30°$ gives $n_e \approx 2.0 \times 10^3\ \mathrm{cm}^{-3}$ and $|\boldsymbol{B}| \approx 11.0$ mG; from Table 4, $N_{\mathrm{CME}} \approx 11.2 \times 10^3\ \mathrm{cm}^{-3}$ and $B_{\mathrm{CME}} \approx 2.4$ mG for CME-3, suggesting an increase in the local plasma density by a factor of ≈ 5.6 and a decrease in the local magnetic-field strength by a factor of about five. In making this comparison, however, it is important to distinguish between the observed structures of CME-1 and CME-2 and the structure of CME-3. CME-1 and CME-2 both have the classic three-part structure, and it is therefore much easier to apply and evaluate the flux-rope model for these two CMEs; CME-3 has a jet-like structure, and whether this is due to geometrical projection effects or because it is a true "narrow" CME, the flux-rope model is more difficult to constrain for this structure. The density enhancement should also be compared to the original plasma-density power-law model as it was given by Sakurai and Spangler (1994a), namely using $N_0 = 1.83 \times 10^6\ \mathrm{cm}^{-3}$, which is an order of magnitude larger than the N_0 determined for each LOS. Evaluating Equation (6) using this value for N_0 as before, we find a more modest increase over the background plasma density by a factor of 3.3, 1.1, and 1.3 for CME-1, CME-2, and CME-3, respectively.

One of the striking features of our results is our ability to represent the background coronal contribution to the observed Faraday rotation using simple single-power-law models for the plasma density and magnetic field. Several models employ two or three power-law terms for the plasma density (*e.g.* see Pätzold *et al.*, 1987) or employ different model parameters depending on the region of the corona that is sampled (*e.g.* see Saito, Poland, and Munro, 1977). Similarly, the magnetic field is often represented by a dual power law in r, such as the sum of a dipole ($\propto r^{-3}$) and interplanetary magnetic field term ($\propto r^{-2}$) (Pätzold *et al.*, 1987; Mancuso and Spangler, 2000; Kooi *et al.*, 2014). The exact form of the power laws assumed in Equations (6) and (8) should not be crucial for the results presented here because different functional forms give similar values for the narrow range of heliocentric distances ($8.0 - 11.4\ \mathrm{R}_\odot$) characteristic of our observations.

Another simplification that we made in modeling the background corona was assuming that the coronal current sheet can be expressed as an infinitely thin magnetic neutral line where the polarity of the radial field reverses. Both Mancuso and Spangler (2000) and Kooi *et al.* (2014) found that accounting for the finite thickness and higher density of this current sheet provided better agreement with the Faraday rotation that they measured. We found excellent agreement between our models and the $\mathrm{RM}(t)$ (before and after occultation by CMEs) without accounting for the thickness or increased density of the current sheet for two reasons: First, our observations were at larger heliocentric distances than those of Kooi *et al.* (2014) and most of the sources observed by Mancuso and Spangler (2000); consequently, the difference between the plasma density inside and outside the current sheet as predicted by the models of, *e.g.*, Mancuso and Spangler (2000) is small. Second, we have assumed that the observed CMEs follow the neutral line out to the heliocentric distances at which we observed, and therefore the plasma structure of the CME would replace the current-sheet structure during CME occultation in our models.

The Faraday-rotation transients associated with CME-1, CME-2, and CME-3 were smaller than those observed by Levy *et al.* (1969) and Cannon, Stelzried, and Ohlson (1973). Two of the transients observed by Levy *et al.* (1969) were at comparable impact parameters (10.9 $R_\odot$ and 8.6 $R_\odot$ on 4 and 8 November 1968, respectively); however, these transients were $\approx 40^\circ$ in amplitude at an observing frequency of 2.292 GHz, which corresponds to RM ≈ 41 rad m^{-2}. This is four times larger than the largest transient that we measured: -11 rad m^{-2}. This is not necessarily surprising because CMEs come in a range of plasma densities and magnetic-field strengths. Cannon, Stelzried, and Ohlson (1973) observed Faraday-rotation transients at smaller impact parameters (see Section 1.4.1), and one such transient displayed an inverse-N shape with a magnitude $|\mathrm{RM}| \approx 7.1$ rad m^{-2}, which is comparable to the three transients that we observed.

Comparison of our data should also be made with the work of Bird *et al.* (1985), in which the measured Faraday-rotation transients were directly associated with the passage of CMEs seen in *Solwind* coronagraph images. In this investigation, Bird *et al.* calculated the weighted mean longitudinal (LOS) component of the magnetic field [$\overline{B}_\mathrm{L}$] associated with the observed transients:

$$\overline{B}_\mathrm{L} = \frac{1}{N_\mathrm{t}} \int_\mathrm{t} n_\mathrm{t} \boldsymbol{B}_\mathrm{t} \cdot \mathrm{d}\boldsymbol{s}, \tag{16}$$

where

$$N_\mathrm{t} = \int_\mathrm{t} n_\mathrm{t} \mathrm{d}s, \tag{17}$$

and t refers to the contribution from the coronal transient. Equations (16) and (17) appear as Equation (8) in Bird *et al.* (1985). Evaluating Equations (16) and (17) for CME-1, CME-2, and CME-3 using the flux-rope model values obtained from observations of 0842, 0843, and 0900 gives a small range in $\overline{B}_\mathrm{L}$: 1 – 6 mG. Our values compare favorably to the values reported in Table 1 of Bird *et al.* (1985), but are smaller than the maximum observed values for $\overline{B}_\mathrm{L}$, reported as 10 – 25 mG in that article. The values in Table 1 of Bird *et al.* (1985) were also calculated for transients located at smaller impact parameters: 4.5 – 7.6 $R_\odot$. Our values are also consistent with the upper limits (< 300 mG) given in Table 1 of Howard *et al.* (2016) for measurements at the beginning of their observations; however, our values exceed the upper limits of Howard *et al.* (2016) (< 0.8 mG) for measurements at the end of their observations by an order of magnitude.

The observations of a coronal Faraday-rotation transient investigated by Ingleby, Spangler, and Whiting (2007) and Spangler and Whiting (2009) had an RM profile similar to 0842: the Faraday rotation, given by Spangler and Whiting (2009) in terms of degrees, at the beginning of the observing session increases slowly from -10° to -5° over three hours and then quickly increases to $+28^\circ$ over the remaining three hours in the observing session. At an observational frequency of 1.465 GHz, this 26° increase corresponds to RM ≈ 10.9 rad m^{-2}, which is comparable to the peak RM measured for 0843, although the source that they observed was much closer to the Sun ($R_0 = 6.6$ $R_\odot$). While the RM(t) is similar to that of 0842, beginning negative before quickly increasing to RM > 0, the CME (Spangler and Whiting, 2009) observed approaching their source did not appear to occult the source in LASCO-C2 images.

The most recent observations reported by Howard *et al.* (2016) demonstrate a dispersion-measure and RM profile similar to the $\mathrm{B_T}(t)$ and RM(t) for 0900, before correcting for the ionospheric contribution to RM. After subtracting an approximation for the ionospheric contribution ($\approx$40% of the observed RM), the RM profile given by Howard *et al.* (2016) resembles the RM(t) for 0843 in shape, although the range of RM that they measure is much smaller (1.7–2.3 rad m^{-2}). While the ionosphere was a significant source of uncertainty in the work of Howard *et al.* (2016), any residual ionospheric Faraday rotation in Figures 7, 8, 9, and 10 in this article is expected to be ≤ 0.1 rad m^{-2} (see Section 2.4) and is therefore negligible.

In modeling the observed CMEs, we assumed a constant density profile for the flux-rope structure. An alternative model is the graduated cylindrical shell (GCS) flux-rope structure of Thernisien, Howard, and Vourlidas (2006), which employs an asymmetric Gaussian profile that requires the electron density to peak at the outer surface of the shell (outer loop) and fall off inside the shell (inner cavity). Applying the GCS model to 34 CMEs from 1997 to 2002, Thernisien, Howard, and Vourlidas (2006) measured peak electron densities of $42-1730 \times 10^3$ cm^{-3}; our measurements for N_{CME} are smaller (Table 4) because assuming a constant density effectively averages the plasma density over the entire structure. This constant density profile is sufficient for modeling the $\mathrm{B_T}(t)$ and $\mathrm{RM}(t)$ for 0843 and 0900 (CME-1 and CME-3, respectively), largely because the LOS only sampled the bright outer loop. The constant density profile does not adequately reproduce the $\mathrm{B_T}(t)$ for 0842, however, because the LOS samples the outer loop and inner cavity of CME-2; in this case, the GCS model would most likely provide a better fit to the data.

The simple flux-rope structure for the magnetic field used in this work is very similar to those employed by Liu *et al.* (2007) and Jensen and Russell (2008), with the exception that we have effectively assumed an infinite axial length and both Liu *et al.* (2007) and Jensen and Russell (2008) placed restrictions on this length. We did not place restrictions on this length because we had restrictions on the geometric parameters θ_{z} and β_{CME} and required $\phi_{\mathrm{z}} = \pm 90° - \beta_{\mathrm{CME}}$ (± referring to sources off the western or eastern limb, respectively) based on LASCO-C3, COR2-A, and COR2-B observations.

While Liu *et al.* (2007) primarily explored differences in predicted RM profiles between different flux-rope models and did not attempt to fit these models to previous observations, the RM predicted by Liu *et al.* (2007) for a model flux rope centered at 10 $\mathrm{R}_\odot$ with an assumed axial field strength of 10 mG is $\approx \pm 9$ rad m^{-2}. This prediction is consistent with both the $\mathrm{RM}(t)$ that we measured for 0843 and the axial field strengths we calculated for CME-1 and CME-2. Furthermore, in trying to model the 23 and 24 October 1979 CMEs observed by Bird *et al.* (1985) at impact parameters of approximately 7.3 $\mathrm{R}_\odot$ and 5.0 $\mathrm{R}_\odot$, respectively, Jensen and Russell (2008) calculated an axial field strength of ≈ 10 mG, which is also consistent with our results.

Despite the simplicity of the constant density profile and the flux-rope magnetic field, the model data fit the observed $\mathrm{B_T}(t)$ and $\mathrm{RM}(t)$ remarkably well, particularly in the case of 0843. This is due in part to our ability to place constraints on the model using observations from LASCO-C3, COR2-A, and COR2-B. The white-light images from LASCO-C3 allow us to estimate the background coronal and CME plasma densities, and the images from COR2-A and COR2-B provide additional vantage points from which we can track the leading edges of the occulting CMEs; this was the primary reason that we could track the leading edges of CME-1 and CME-2 as they occulted 0843. In modeling the data for 0843, we also made use of the independent measurements for 0842; without this additional LOS, modeling the effects of two CMEs would have proven much more difficult. These results underscore the power of performing Faraday-rotation observations of CMEs with multiple LOS to multiple sources.

A significant improvement over these observations would require a set of VLA observations that are triggered in the event of a CME displaying favorable geometry (*e.g.* exhibiting the three-part structure and originating on or near the solar limb). An effective trigger would be near real-time LASCO-C2 data. An image with adequate quality to identify an emerging

CME is available at a time that is, at most, one hour before present. These near real-time data are sufficient to detect CMEs when they are still low in the corona so that one may predict i) the position angle of their eruption and ii) the approximate time of arrival at heliocentric distances of 5 – 20 $R_\odot$. For a set of triggered observations, 8 – 9 strongly polarized extended sources could be selected that are certain to be directly occulted by a CME. In order to confirm or refute the flux-rope model or distinguish between force-free and non-force-free flux-rope models, it is imperative that there are several LOS through the three-part structure of the CME, ideally with at least one LOS along the CME's axis of symmetry.

6. Summary and Conclusions

i) We performed polarimetric observations using the newly upgraded VLA of a constellation of extragalactic radio sources for six hours on 2 August, 5 August, and 19 August 2012, at heliocentric distances (our parameter R_0) ranging over 5 – 15 $R_\odot$. During the 2 August session, three radio sources were occulted by CMEs: 0842, 0843, and 0900. Ten scans of three to four minutes duration were made of each source at frequencies of 1 – 2 GHz. The data were reduced using the Common Astronomy Software Applications (CASA) data-reduction package with the new ionospheric Faraday-rotation correction algorithm that Jason Kooi and George Moellenbrock implemented. These observations represent the first active hunt for CME Faraday rotation using the VLA.

ii) In addition to our radioastronomical observations, we obtained white-light coronagraph images from the LASCO-C3 instrument onboard SOHO to determine the Thomson-scattering brightness [B_T] along the LOS to each source. The B_T is proportional to the electron plasma density sampled by the LOS and provides a means to independently estimate the plasma density and determine its contribution to the observed Faraday rotation.

iii) We determined the Thomson-scattering time series [$B_T(t)$] and rotation-measure time series [$RM(t)$] for each source occulted by a CME as well as for one source, 0846, that was only occulted by the coronal plasma. Large coronal transients that exceeded nominal coronal values were observed in both $B_T(t)$ and $RM(t)$ for 0842, 0843, and 0900 (Figures 8 – 10). By contrast, the source that was only occulted by the corona did not demonstrate deviations from the $B_T(t)$ and $RM(t)$ expected for the background corona (Figure 7).

iv) A single-power-law model was used for the background coronal plasma density and magnetic field. This proved sufficient to reproduce the observed $B_T(t)$ and $RM(t)$ for 0846 as well as the other sources before occultation by a CME; however, our values for N_0 (Table 3) are lower than the original model value of $N_0 = 1.83 \times 10^6\ \mathrm{cm}^{-3}$ used by Sakurai and Spangler (1994a) and subsequent work. The agreement between the background coronal model and data for 0900 are particularly important as they demonstrate the necessity of accounting for the LOS crossing multiple magnetic neutral lines; furthermore, this agreement demonstrates that our models for the background coronal RM are not systematically biased toward negative values. The ability to properly model the background corona is crucial in identifying and measuring CME-related transients.

v) A constant-density force-free flux rope embedded in the background corona was used to model the effects of the CMEs on $B_T(t)$ and $RM(t)$. In the case of 0842, the flux-rope model underestimated the peak value of $B_T(t)$ and did not predict the decreasing $B_T(t)$ inside the inner cavity region of the CME; however, there was satisfactory agreement between the model and the $RM(t)$ (in particular, the model reproduces the sign change and gradual slope, Figure 8). For 0900, the single-flux-rope model successfully reproduces both the observed $B_T(t)$ and $RM(t)$ profiles (Figure 9).

vi) 0843 was occulted by two CMEs on 2 August 2012, as verified in STEREO-A COR2 images, and therefore the coronal transient observed in $B_T(t)$ and $RM(t)$ cannot be satisfactorily modeled with a single flux rope; consequently, we modeled observations of 0843 using two flux ropes embedded in the background corona. The introduction of a second flux rope is not merely the introduction of more free parameters, but it is *required* to account for the second CME. Furthermore, we used the model parameters determined from the independent measurements of 0842 for the second CME to predict the $B_T(t)$ and $RM(t)$ resulting from the two-flux-rope model. This two-flux-rope model successfully reproduces both the $B_T(t)$ and $RM(t)$ for 0843 (Figure 10). In particular, the two-flux-rope model successfully replicates the appropriate slope in $RM(t)$ before and after occultation by the second CME and predicts the observed change in sign to $RM > 0$ at the end of the observing session.

vii) The Faraday-rotation transients that we measured were smaller than those observed by Levy *et al.* (1969) and Cannon, Stelzried, and Ohlson (1973) and larger than those observed by Howard *et al.* (2016); however, the plasma densities ($6 - 22 \times 10^3\ \mathrm{cm}^{-3}$) and axial magnetic-field strengths (2 – 12 mG) inferred from our models are consistent with the model predictions of Liu *et al.* (2007) and axial magnetic-field strengths inferred by Jensen and Russell (2008). Furthermore, the weighted mean LOS component of the magnetic field calculated from our data gives 1 – 6 mG, in agreement with the results of Bird *et al.* (1985).

Acknowledgments This work was supported at the University of Iowa by grants ATM09-56901 and AST09-07911 from the National Science Foundation and supported at the U.S. Naval Research Laboratory by the Jerome and Isabella Karle Distinguished Scholar Fellowship program. The SOHO/LASCO data used here are produced by a consortium of the Naval Research Laboratory (USA), Max-Planck-Institut für Aeronomie (Germany), Laboratoire d'Astronomie (France), and the University of Birmingham (UK). SOHO is a project of international cooperation between ESA and NASA. We thank George Moellenbrock of the NRAO staff for his patience and assistance in implementing ionospheric Faraday-rotation corrections in CASA. We also thank the referee, whose comments and suggestions improved the content and overall presentation of this article.

Disclosure of Potential Conflicts of Interest The authors declare that they have no conflicts of interest.

References

Andreev, V.E., Efimov, A.I., Samoznaev, L.N., Chashei, I.V., Bird, M.K.: 1997, Characteristics of coronal Alfven waves deduced from HELIOS Faraday rotation measurements. *Solar Phys.* **176**, 387. DOI. ADS.

Babcock, H.W.: 1961, The topology of the Sun's magnetic field and the 22-year cycle. *Astrophys. J.* **133**, 572. DOI. ADS.

Banaszkiewicz, M., Axford, W.I., McKenzie, J.F.: 1998, An analytic solar magnetic field model. *Astron. Astrophys.* **337**, 940. ADS.

Bignell, C.: 1982, Polarimetry. In: Thompson, A.R., D'Addario, L.R. (eds.) *Synthesis Mapping*, National Radio Astronomy Observatory, Green Bank, 6. ADS.

Bird, M.K.: 2007, Coronal Faraday rotation of occulted radio signals. *Astron. Astrophys. Trans.* **26**, 441. DOI. ADS.

Bird, M.K., Edenhofer, P.: 1990, In: Schwenn, R., Marsch, E. (eds.) *Remote Sensing Observations of the Solar Corona*, Springer, Berlin, 13. ADS.

Bird, M.K., Schruefer, E., Volland, H., Sieber, W.: 1980, Coronal Faraday rotation during solar occultation of PSR0525+21. *Nature* **283**, 459. DOI. ADS.

Bird, M.K., Volland, H., Howard, R.A., Koomen, M.J., Michels, D.J., Sheeley, N.R. Jr., Amstrong, J.W., Seidel, B.L., Stelzried, C.T., Woo, R.: 1985, White-light and radio sounding observations of coronal transients. *Solar Phys.* **98**, 341. DOI. ADS.

Brueckner, G.E.: 1974, The behaviour of the outer solar corona (3 $R_\odot$ to 10 $R_\odot$) during a large solar flare observed from OSO-7 in white light. In: Newkirk, G.A. (ed.) *Coronal Disturbances*, *IAU Symp.* **57**, Reidel, Dordrecht, 333. ADS.

Brueckner, G.E., Howard, R.A., Koomen, M.J., Korendyke, C.M., Michels, D.J., Moses, J.D., Socker, D.G., Dere, K.P., Lamy, P.L., Llebaria, A., Bout, M.V., Schwenn, R., Simnett, G.M., Bedford, D.K., Eyles, C.J.: 1995, The Large Angle Spectroscopic Coronagraph (LASCO). *Solar Phys.* **162**, 357. DOI. ADS.

Burlaga, L.F.: 1988, Magnetic clouds and force-free fields with constant alpha. *J. Geophys. Res.* **93**, 7217. DOI. ADS.

Burlaga, L., Sittler, E., Mariani, F., Schwenn, R.: 1981, Magnetic loop behind an interplanetary shock – voyager, helios, and IMP 8 observations. *J. Geophys. Res.* **86**, 6673. DOI. ADS.

Cannon, A.R., Stelzried, C.T., Ohlson, J.E.: 1973, Faraday rotation observations during the 1970 pioneer 9 solar occultation. *Deep Space Netw. Prog. Rep.* **16**, 87. ADS.

Chen, J.: 1996, Theory of prominence eruption and propagation: interplanetary consequences. *J. Geophys. Res.* **101**, 27499. DOI. ADS.

Chen, P.F.: 2011, Coronal mass ejections: models and their observational basis. *Living Rev. Solar Phys.* **8**, 1. DOI. ADS.

Colaninno, R.C., Vourlidas, A.: 2009, First determination of the true mass of coronal mass ejections: a novel approach to using the two STEREO viewpoints. *Astrophys. J.* **698**, 852. DOI. ADS.

Colaninno, R.C., Vourlidas, A.: 2015, Using multiple-viewpoint observations to determine the interaction of three coronal mass ejections observed on 2012 March 5. *Astrophys. J.* **815**, 70. DOI. ADS.

Condon, J.J., Cotton, W.D., Greisen, E.W., Yin, Q.F., Perley, R.A., Taylor, G.B., Broderick, J.J.: 1998, The NRAO VLA sky survey. *Astron. J.* **115**, 1693. DOI. ADS.

Domingo, V., Fleck, B., Poland, A.I.: 1995, The SOHO mission: an overview. *Solar Phys.* **162**, 1. DOI. ADS.

Efimov, A.I., Lukanina, L.A., Rogashkova, A.I., Samoznaev, L.N., Chashei, I.V., Bird, M.K., Pätzold, M.: 2015, Coronal radio occultation experiments with the helios solar probes: correlation/spectral analysis of Faraday rotation fluctuations. *Solar Phys.* **290**, 2397. DOI. ADS.

Gibson, S.E., Low, B.C.: 1998, A time-dependent three-dimensional magnetohydrodynamic model of the coronal mass ejection. *Astrophys. J.* **493**, 460. DOI. ADS.

Gibson, S.E., Low, B.C.: 2000, Three-dimensional and twisted: an MHD interpretation of on-disk observational characteristics of coronal mass ejections. *J. Geophys. Res.* **105**, 18187. DOI. ADS.

Gibson, S.E., Foster, D., Burkepile, J., de Toma, G., Stanger, A.: 2006, The calm before the storm: the link between quiescent cavities and coronal mass ejections. *Astrophys. J.* **641**, 590. DOI. ADS.

Gleeson, L.J., Axford, W.I.: 1976, An analytic model illustrating the effects of rotation on a magnetosphere containing low-energy plasma. *J. Geophys. Res.* **81**, 3403. DOI. ADS.

Gopalswamy, N., Yashiro, S., Michalek, G., Stenborg, G., Vourlidas, A., Freeland, S., Howard, R.: 2009, The SOHO/LASCO CME catalog. *Earth Moon Planets* **104**, 295. DOI. ADS.

Gosling, J.T., Hildner, E., MacQueen, R.M., Munro, R.H., Poland, A.I., Ross, C.L.: 1974, Mass ejections from the sun – a view from SKYLAB. *J. Geophys. Res.* **79**, 4581. DOI. ADS.

Gosling, J.T., McComas, D.J., Phillips, J.L., Bame, S.J.: 1991, Geomagnetic activity associated with Earth passage of interplanetary shock disturbances and coronal mass ejections. *J. Geophys. Res.* **96**, 7831. DOI. ADS.

Gurnett, D.A., Bhattacharjee, A.: 2006, *Introduction to Plasma Physics*, Cambridge University, Cambridge.

Hayes, A.P., Vourlidas, A., Howard, R.A.: 2001, Deriving the electron density of the solar corona from the inversion of total brightness measurements. *Astrophys. J.* **548**, 1081. DOI. ADS.

Hollweg, J.V., Bird, M.K., Volland, H., Edenhofer, P., Stelzried, C.T., Seidel, B.L.: 1982, Possible evidence for coronal Alfven waves. *J. Geophys. Res.* **87**, 1. DOI. ADS.

Howard, R.A., Moses, J.D., Vourlidas, A., Newmark, J.S., Socker, D.G., Plunkett, S.P., Korendyke, C.M., Cook, J.W., Hurley, A., Davila, J.M., Thompson, W.T., St Cyr, O.C., Mentzell, E., Mehalick, K., Lemen, J.R., Wuelser, J.P., Duncan, D.W., Tarbell, T.D., Wolfson, C.J., Moore, A., Harrison, R.A., Waltham, N.R., Lang, J., Davis, C.J., Eyles, C.J., Mapson-Menard, H., Simnett, G.M., Halain, J.P., Defise, J.M., Mazy, E., Rochus, P., Mercier, R., Ravet, M.F., Delmotte, F., Auchere, F., Delaboudiniere, J.P., Bothmer, V., Deutsch, W., Wang, D., Rich, N., Cooper, S., Stephens, V., Maahs, G., Baugh, R., McMullin, D., Carter, T.: 2008, Sun Earth Connection Coronal and Heliospheric Investigation (SECCHI). *Space Sci. Rev.* **136**, 67. DOI. ADS.

Howard, T.A., Stovall, K., Dowell, J., Taylor, G.B., White, S.M.: 2016, Measuring the magnetic field of coronal mass ejections near the Sun using pulsars. *Astrophys. J.* **831**, 208. DOI. ADS.

Illing, R.M.E., Hundhausen, A.J.: 1985, Observation of a coronal transient from 1.2 to 6 solar radii. *J. Geophys. Res.* **90**, 275. DOI. ADS.

Ingleby, L.D., Spangler, S.R., Whiting, C.A.: 2007, Probing the large-scale plasma structure of the solar corona with Faraday rotation measurements. *Astrophys. J.* **668**, 520. DOI. ADS.

Jensen, E.A., Russell, C.T.: 2008, Faraday rotation observations of CMEs. *Geophys. Res. Lett.* **35**, L02103. DOI. ADS.

Jensen, E.A., Bisi, M.M., Breen, A.R., Heiles, C., Minter, T., Vilas, F.: 2013a, Measurements of Faraday rotation through the solar corona during the 2009 solar minimum with the MESSENGER spacecraft. *Solar Phys.* **285**, 83. DOI. ADS.

Jensen, E.A., Nolan, M., Bisi, M.M., Chashei, I., Vilas, F.: 2013b, MESSENGER observations of magnetohydrodynamic waves in the solar corona from Faraday rotation. *Solar Phys.* **285**, 71. DOI. ADS.

Jensen, E.A., Frazin, R., Heiles, C., Lamy, P., Llebaria, A., Anderson, J.D., Bisi, M.M., Fallows, R.A.: 2016, The comparison of total electron content between radio and Thompson scattering. *Solar Phys.* **291**, 465. DOI. ADS.

Kaiser, M.L., Kucera, T.A., Davila, J.M., St. Cyr, O.C., Guhathakurta, M., Christian, E.: 2008, The STEREO mission: an introduction. *Space Sci. Rev.* **136**, 5. DOI. ADS.

Kooi, J.E.: 2016, Very Large Array Faraday Rotation Studies of the Coronal Plasma. PhD thesis, University of Iowa.

Kooi, J.E., Fischer, P.D., Buffo, J.J., Spangler, S.R.: 2014, Measurements of coronal Faraday rotation at 4.6 $R_\odot$. *Astrophys. J.* **784**, 68. DOI. ADS.

Le Chat, G., Kasper, J.C., Cohen, O., Spangler, S.R.: 2014, Diagnostics of the solar corona from comparison between Faraday rotation measurements and magnetohydrodynamic simulations. *Astrophys. J.* **789**, 163. DOI. ADS.

Lepping, R.P., Burlaga, L.F., Jones, J.A.: 1990, Magnetic field structure of interplanetary magnetic clouds at 1 AU. *J. Geophys. Res.* **95**, 11957. DOI. ADS.

Levy, G.S., Sato, T., Seidel, B.L., Stelzried, C.T., Ohlson, J.E., Rusch, W.V.T.: 1969, Pioneer 6: measurement of transient Faraday rotation phenomena observed during solar occultation. *Science* **166**, 596. DOI. ADS.

Liu, Y., Manchester, W.B. IV, Kasper, J.C., Richardson, J.D., Belcher, J.W.: 2007, Determining the magnetic field orientation of coronal mass ejections from Faraday rotation. *Astrophys. J.* **665**, 1439. DOI. ADS.

Low, B.C.: 2001, Coronal mass ejections, magnetic flux ropes, and solar magnetism. *J. Geophys. Res.* **106**, 25141. DOI. ADS.

MacQueen, R.M., Eddy, J.A., Gosling, J.T., Hildner, E., Munro, R.H., Newkirk, G.A. Jr., Poland, A.I., Ross, C.L.: 1974, The outer solar corona as observed from skylab: preliminary results. *Astrophys. J. Lett.* **187**, L85. DOI. ADS.

Mancuso, S., Garzelli, M.V.: 2013, Radial profile of the inner heliospheric magnetic field as deduced from Faraday rotation observations. *Astron. Astrophys.* **553**, A100. DOI. ADS.

Mancuso, S., Spangler, S.R.: 1999, Coronal Faraday rotation observations: measurements and limits on plasma inhomogeneities. *Astrophys. J.* **525**, 195. DOI. ADS.

Mancuso, S., Spangler, S.R.: 2000, Faraday rotation and models for the plasma structure of the solar corona. *Astrophys. J.* **539**, 480. DOI. ADS.

McMullin, J.P., Waters, B., Schiebel, D., Young, W., Golap, K.: 2007, CASA architecture and applications. In: Shaw, R.A., Hill, F., Bell, D.J. (eds.) *Astronomical Data Analysis Software and Systems XVI* **CS-376**, Astron. Soc. Pacific, San Francisco, 127. ADS.

Mierla, M., Inhester, B., Antunes, A., Boursier, Y., Byrne, J.P., Colaninno, R., Davila, J., de Koning, C.A., Gallagher, P.T., Gissot, S., Howard, R.A., Howard, T.A., Kramar, M., Lamy, P., Liewer, P.C., Maloney, S., Marqué, C., McAteer, R.T.J., Moran, T., Rodriguez, L., Srivastava, N., St. Cyr, O.C., Stenborg, G., Temmer, M., Thernisien, A., Vourlidas, A., West, M.J., Wood, B.E., Zhukov, A.N.: 2010, On the 3-D reconstruction of coronal mass ejections using coronagraph data. *Ann. Geophys.* **28**, 203. DOI. ADS.

Morrill, J.S., Howard, R.A., Vourlidas, A., Webb, D.F., Kunkel, V.: 2009, The impact of geometry on observations of CME brightness and propagation. *Solar Phys.* **259**, 179. DOI. ADS.

Olmedo, O., Zhang, J., Wechsler, H., Poland, A., Borne, K.: 2008, Automatic detection and tracking of coronal mass ejections in coronagraph time series. *Solar Phys.* **248**, 485. DOI. ADS.

Ord, S.M., Johnston, S., Sarkissian, J.: 2007, The magnetic field of the solar corona from pulsar observations. *Solar Phys.* **245**, 109. DOI. ADS.

Pätzold, M., Bird, M.K.: 1998, The pioneer 6 Faraday rotation transients-on the interpretation of coronal Faraday rotation data. *Geophys. Res. Lett.* **25**, 2105. DOI. ADS.

Pätzold, M., Bird, M.K., Volland, H., Levy, G.S., Seidel, B.L., Stelzried, C.T.: 1987, The mean coronal magnetic field determined from HELIOS Faraday rotation measurements. *Solar Phys.* **109**, 91. DOI. ADS.

Robbrecht, E., Berghmans, D., Van der Linden, R.A.M.: 2009, Automated LASCO CME catalog for solar cycle 23: are CMEs scale invariant? *Astrophys. J.* **691**, 1222. DOI. ADS.

Saito, K., Poland, A.I., Munro, R.H.: 1977, A study of the background corona near solar minimum. *Solar Phys.* **55**, 121. DOI. ADS.

Sakurai, T., Spangler, S.R.: 1994a, The study of coronal plasma structures and fluctuations with Faraday rotation measurements. *Astrophys. J.* **434**, 773. DOI. ADS.

Sakurai, T., Spangler, S.R.: 1994b, Use of the very large array for measurement of time variable Faraday rotation. *Radio Sci.* **29**, 635. DOI. ADS.

Schwenn, R.: 2006, Space weather: the solar perspective. *Living Rev. Solar Phys.* **3**, 2. DOI. ADS.

Soboleva, N.S., Timofeeva, G.M.: 1983, The Faraday effect in the solar supercorona during its 1977 – 1982 radio occultations of the crab nebula. *Sov. Astron. Lett.* **9**, 216. ADS.

Sofue, Y., Kawabata, K., Kawajiri, N., Kawano, N.: 1972, Faraday rotation of linearly polarized radio waves from the crab nebula by the solar corona. *Publ. Astron. Soc. Japan* **24**, 309. ADS.

Spangler, S.R.: 2005, The strength and structure of the coronal magnetic field. *Space Sci. Rev.* **121**, 189. DOI. ADS.

Spangler, S.R., Whiting, C.A.: 2009, Radio remote sensing of the corona and the solar wind. In: Gopalswamy, N., Webb, D.F. (eds.) *IAU Symp.* **257**, 529. DOI. ADS.

Stelzried, C.T., Levy, G.S., Sato, T., Rusch, W.V.T., Ohlson, J.E., Schatten, K.H., Wilcox, J.M.: 1970, The quasi-stationary coronal magnetic field and electron density as determined from a Faraday rotation experiment. *Solar Phys.* **14**, 440. DOI. ADS.

Thernisien, A.F.R., Howard, R.A., Vourlidas, A.: 2006, Modeling of flux rope coronal mass ejections. *Astrophys. J.* **652**, 763. DOI. ADS.

van de Hulst, H.C.: 1950, The electron density of the solar corona. *Bull. Astron. Inst. Neth.* **11**, 135. ADS.

Vogt, M.F., Cohen, D.M.S., Puhl-Quinn, P., Jordanova, V.K., Smith, C.W., Skoug, R.M.: 2006, Space weather drivers in the ACE era. *Space Weather* **4**, S09001. DOI. ADS.

Vourlidas, A., Howard, R.A.: 2006, The proper treatment of coronal mass ejection brightness: a new methodology and implications for observations. *Astrophys. J.* **642**, 1216. DOI. ADS.

Vourlidas, A., Howard, R.A., Esfandiari, E., Patsourakos, S., Yashiro, S., Michalek, G.: 2010, Comprehensive analysis of coronal mass ejection mass and energy properties over a full solar cycle. *Astrophys. J.* **722**, 1522. DOI. ADS.

Weimer, D.R., Ober, D.M., Maynard, N.C., Burke, W.J., Collier, M.R., McComas, D.J., Ness, N.F., Smith, C.W.: 2002, Variable time delays in the propagation of the interplanetary magnetic field. *J. Geophys. Res.* **107**, A81210. DOI. ADS.

Wood, B.E., Howard, R.A., Thernisien, A., Plunkett, S.P., Socker, D.G.: 2009, Reconstructing the 3D morphology of the 17 May 2008 CME. *Solar Phys.* **259**, 163. DOI. ADS.

You, X.P., Coles, W.A., Hobbs, G.B., Manchester, R.N.: 2012, Measurement of the electron density and magnetic field of the solar wind using millisecond pulsars. *Mon. Not. Roy. Astron. Soc.* **422**, 1160. DOI. ADS.